

Calibration of macroscopic first-order traffic flow models for lane-free automated vehicle traffic

DIPLOMA THESIS

by

Konstantinos Mitrakas

supervisor

Prof. Ioannis Papamichail

*A thesis submitted in fulfillment of the requirements for the
diploma of Production Engineering and Management in the
Dynamic Systems and Simulation Laboratory*

Chania, Greece

September, 2024

This page is internationally left blank.

Abstract

A novel traffic paradigm, called TrafficFluid, was recently proposed for automated vehicles. It is characterized by two integrated principles: lane-free traffic and vehicle nudging. The latter suggests that vehicles can be influenced (nudged) by other vehicles in their vicinity, even behind them. Various vehicle movement strategies have been designed for this concept that can be employed for microscopic traffic simulation. On the other hand, macroscopic models may be used to produce large-scale simulation results with low computational effort, but also to gain insights on the emerging macroscopic properties of lane-free traffic with vehicle nudging. Furthermore, macroscopic models can be used for various significant traffic engineering tasks, including estimation and control strategy design.

This thesis employs an ad-hoc vehicle movement strategy for Connected and Automated Vehicles (CAVs) driving in a lane-free highway environment, to produce data that can be utilized to calibrate macroscopic models. Four macroscopic models, original CTM, extended version of CTM, drivers' anticipation model and an extended version of drivers' anticipation model, are calibrated to fit the data, and optimal model parameters are determined for different highway widths and different vehicle nudging levels. The previously developed CALISTO software tool and its GUI are appropriately extended to handle the new models. These models include an anticipation term that influences the total outflow from a highway section according to the downstream prevailing conditions. This mechanism suggests that drivers adjust their speed, by also considering the downstream density. Moreover, in the space-discretised version, the traffic volume considered in the conservation equation is a convex combination of the total traffic volume of the current, the next and the previous sections.

The traffic conditions observed in the microscopic lane-free CAV traffic have been reproduced with sufficient accuracy. Highway capacity and critical density have shown a linear increase as the highway width expands, with further increases observed when vehicle nudging is elevated. However, free speed remains unaffected by highway width and has only shown a slight increase with vehicle nudging.

Περίληψη

Πρόσφατα προτάθηκε ένα νέο παράδειγμα κυκλοφορίας, με το όνομα TrafficFluid, για αυτοματοποιημένα οχήματα. Το συγκεκριμένο παράδειγμα χαρακτηρίζεται από δύο βασικές αρχές: την κυκλοφορία χωρίς λωρίδες και την ιδιότητα ώθησης οχημάτων. Η τελευταία υποδηλώνει ότι τα οχήματα μπορούν να επηρεαστούν (υποστούν ώθηση) από άλλα οχήματα που βρίσκονται κοντά τους, ακόμη και πίσω τους. Για την έννοια αυτή έχουν σχεδιαστεί ποικίλες στρατηγικές κίνησης οχημάτων που μπορούν να αξιοποιηθούν για την μικροσκοπική προσομοίωση της κυκλοφορίας. Από την άλλη πλευρά, τα μακροσκοπικά μοντέλα μπορούν να χρησιμοποιηθούν για την παραγωγή αποτελεσμάτων προσομοίωσης μεγάλης κλίμακας με χαμηλή υπολογιστική προσπάθεια, αλλά και για την απόκτηση γνώσεων σχετικά με τις αναδυόμενες μακροσκοπικές ιδιότητες της κυκλοφορίας σε δίκτυο χωρίς λωρίδες λαμβάνοντας υπόψη την ώθηση των οχημάτων. Επιπλέον, τα μακροσκοπικά μοντέλα μπορούν να χρησιμοποιηθούν για διάφορες σημαντικές πτυχές της κυκλοφοριακής τεχνικής, συμπεριλαμβανομένης της εκτίμησης και του σχεδιασμού στρατηγικών ελέγχου.

Η παρούσα διπλωματική εργασία χρησιμοποιεί μια ad-hoc στρατηγική κίνησης οχημάτων για συνδεδεμένα και αυτοματοποιημένα οχήματα (CAV) που κινούνται σε περιβάλλον αυτοκινητόδρομου χωρίς λωρίδες κυκλοφορίας, με σκοπό την παραγωγή δεδομένων που μπορούν να χρησιμοποιηθούν για την βαθμονόμηση μακροσκοπικών μοντέλων. Τέσσερα μακροσκοπικά μοντέλα, το original CTM, μια εκδοχή του original CTM, ένα μοντέλο με έναν παράγοντα πρόβλεψης των οδηγών και μια εκτεταμένη εκδοχή του συγκεκριμένου μοντέλου, βαθμονομούνται ώστε να προσαρμοστούν στα δεδομένα, με στόχο τον προσδιορισμό των βέλτιστων παραμέτρων για διαφορετικά πλάτη αυτοκινητοδρόμων και διαφορετικά επίπεδα ώθησης οχημάτων. Το εργαλείο λογισμικού CALISTO, που είχε αναπτυχθεί προηγουμένως, και το γραφικό περιβάλλον χρήσης του επεκτείνονται κατάλληλα για να χειριστούν τα νέα μοντέλα. Αυτά τα νέα μοντέλα περιλαμβάνουν έναν όρο πρόβλεψης που επηρεάζει την συνολική εκροή από ένα τμήμα του αυτοκινητοδρόμου ανάλογα με τις επικρατούσες συνθήκες καταντή. Ο μηχανισμός αυτός υποδηλώνει ότι οι οδηγοί προσαρμόζουν την ταχύτητά τους, λαμβάνοντας επίσης υπόψη την πυκνότητα καταντή. Επιπλέον, στην εκδοχή με διακριτό χώρο, η κυκλοφοριακή ροή που λαμβάνεται υπόψη στην εξίσωση διατήρησης

είναι ένας κυρτός συνδυασμός της συνολικής ροής του τρέχοντος, του επόμενου και του προηγούμενου τμήματος.

Προέκυψε ότι οι συνθήκες κυκλοφορίας που παρατηρούνται στην κυκλοφορία χωρίς λωρίδες με CAV σε μικροσκοπικό επίπεδο αναπαρίστανται με επαρκή ακρίβεια. Η χωρητικότητα του αυτοκινητοδρόμου και η κρίσιμη πυκνότητα αποδείχτηκε ότι αυξάνονται γραμμικά με την αύξηση του πλάτους του αυτοκινητοδρόμου και υπάρχει περαιτέρω αύξηση των ίδιων μεγεθών για αυξημένα επίπεδα ώθησης των οχημάτων. Από την άλλη πλευρά, η ελεύθερη ταχύτητα είναι ανεξάρτητη από το πλάτος του αυτοκινητόδρομου και αυξάνεται ελαφρώς με την ανάλογη ώθηση των οχημάτων.

Acknowledgements

First and foremost, I would like to thank my supervisor Professor Ioannis Papamichail for trusting me to become a member of the Dynamic Systems and Simulation Laboratory and carry out my thesis in the context of an on-going research project, called TrafficFluid. I owe special thanks to Vasileios Markantonakis, member of the Lab, for his patience and his valuable knowledge and guidance during my first steps in the laboratory.

I would like to express my deepest gratitude to my parents and my sister, whose unwavering support has guided me through both the highs and lows of this challenging yet rewarding journey. The person I am today is largely a reflection of their influence and encouragement.

I also want to extend my heartfelt thanks to my dear friends, Glykeria, Evripidis, Dimitris, Nikos, Giorgos, Asteris and Konstantinos with whom I've shared this journey over the past five years. The cherished memories and countless conversations we've had will stay with me always. I'm truly grateful to have crossed paths with such remarkable people—until our next reunion, I look forward to more good times together.

Contents

Chapter 1- Introduction	1
1.1 Motivation.....	1
1.2 Traffic Fluid.....	2
1.3 Thesis Objectives	3
1.4 Thesis Outlines	4
Chapter 2 - The Microscopic World.....	5
2.1 Vehicle Moving Strategy.....	5
2.2 Forces.....	6
2.2.1 Target - Speed Forces.....	7
2.2.2 Repulsive and Nudging Forces	8
Chapter 3 - The Macroscopic World	10
3.1 Macroscopic vs. Microscopic Models	10
3.2 Fundamental Diagram.....	10
3.3 LWR model.....	13
3.4 Cell Transmission Model and Extended Version	15
3.5 First Order Model with Driver's Anticipation	18
3.5.1 Explanation of Code for the Model with Driver's Anticipation in C++	21
3.6 Extended Version of Drivers Anticipation Model.....	22
3.6.1 Explanation of Code for the Extended Version of Drivers Anticipation Model in C++.....	24

Chapter 4 - Traffic Flow Model Calibration	25
4.1 Calibration Procedure	25
4.2 Nelder-Mead Algorithm.....	28
4.3 CALISTO Tool	30
4.3.1 CALISTO Interface Window	31
 Chapter 5 - Implementation.....	 32
5.1 Microscopic Simulation Set up and Traffic Data.....	32
5.2 The Calibration Procedure in CALISTO	34
 Chapter 6 - Results.....	 36
6.1 Simulations of Original CTM	36
6.2 Simulations of Extended Version of CTM.....	42
6.3 Simulations of First Order Model with Driver's Anticipation.....	48
6.4 Simulations of Extended Version of Drivers Anticipation Model	54
6.5 The Overall Comparison of Results.....	61
 Chapter 7- Conclusion.....	 63

List of Figures

Figure 1.1: The layout of a lane-free highway.

Figure 1.2: The principle of vehicle nudging.

Figure 2.1: Visualization of repulsive and nudging forces between two vehicles.

Figure 2.2: The target-speed forces providing deceleration or acceleration, as needed, to address deviations from a desired speed.

Figure 2.3: The graphical depiction of function $H(\Delta y, L_y, D_y)$.

Figure 2.4: Action Graph depicting the acceleration strategy based on the longitudinal distance and relative speed between vehicles j and i .

Figure 3.1: A general graphical representation of the relationship between speed and density.

Figure 3.2: A general graphical representation of the relationship between flow and density.

Figure 3.3: The triangular FD of original CTM.

Figure 3.4: The illustration of the actual flow from section i to section $i + 1$ at drivers' anticipation model.

Figure 3.5: The illustration of the actual flow from section i to section $i + 1$ at the extended version of drivers' anticipation model.

Figure 4.1: Flow chart describing how the calibration procedure works.

Figure 4.2: The graphical representation of the simplex, illustrating the available transformations within the algorithm, includes reflection, contraction, expansion, and shrink.

Figure 4.3: The window's interface of CALISTO.

Figure 5.1: A schematic representation of the highway sections utilized for the simulations with the off-ramp located at S5 and the on-ramp located at S7.

Figure 5.2: A snapshot of the TrafficFluid-Sim software.

Figure 6.1: Space-time diagrams of microscopically produced speed (ground truth) versus macroscopic model estimates (model) for highway width of 8.5 m and no nudging for original CTM.

Figure 6.2: Space-time diagrams of microscopically produced flow (ground truth) versus macroscopic model estimates (model) for highway width of 8.5 m and no nudging for original CTM.

Figure 6.3: Space-time diagrams of microscopically produced flow (ground truth) versus macroscopic model estimates (model) for highway width of 10.2 m and half nudging for original CTM.

Figure 6.4: Space-time diagrams of microscopically produced speed (ground truth) versus macroscopic model estimates (model) for highway width of 10.2 m and half nudging for original CTM.

Figure 6.5: Line graph representing the model's objective function values based on the various highway widths and nudging scenarios (No nudging, Half nudging, and Full nudging) for original CTM.

Figure 6.6: Critical density versus highway width for full, weak, and no nudging for original CTM.

Figure 6.7: Capacity versus highway width for full, weak, and no nudging for original CTM.

Figure 6.8: Free flow speed versus highway width for full, weak, and no nudging for original CTM.

Figure 6.10: Space-time diagrams of microscopically produced speed (ground truth) versus macroscopic model estimates (model) for highway width of 10.2 m and half nudging for extended version of CTM.

Figure 6.9: Space-time diagrams of microscopically produced flow (ground truth) versus macroscopic model estimates (model) for highway width of 10.2 m and half nudging for extended version of CTM.

Figure 6.11: Space-time diagrams of microscopically produced speed (ground truth) versus macroscopic model estimates (model) for highway width of 11.9 m and full nudging for extended version of CTM.

Figure 6.12: Space-time diagrams of microscopically produced flow (ground truth) versus macroscopic model estimates (model) for highway width of 11.9 m and full nudging for extended version of CTM.

Figure 6.13: Line graph representing the model's objective function values based on the various highway widths and nudging scenarios (No nudging, Half nudging, and Full nudging) for extended version of CTM.

Figure 6.14: Critical density versus highway width for full, weak, and no nudging for extended version of CTM.

Figure 6.16: Capacity versus highway width for full, weak, and no nudging for extended version of CTM.

Figure 6.15: Free flow speed versus highway width for full, weak, and no nudging for extended version of CTM.

Figure 6.17: Space-time diagrams of microscopically produced flow (ground truth) versus macroscopic model estimates (model) for highway width of 8.5 m and no nudging for driver's anticipation model.

Figure 6.18: Space-time diagrams of microscopically produced speed (ground truth) versus macroscopic model estimates (model) for highway width of 8.5 m and no nudging for driver's anticipation model.

Figure 6.19: Space-time diagrams of microscopically produced flow (ground truth) versus macroscopic model estimates (model) for highway width of 11.9 m and full nudging for driver's anticipation model.

Figure 6.20: Space-time diagrams of microscopically produced speed (ground truth) versus macroscopic model estimates (model) for highway width of 11.9 m and full nudging for driver's anticipation model.

Figure 6.21: Line graph representing the model's objective function values based on the various highway widths and nudging scenarios (No nudging, Half nudging, and Full nudging) for driver's anticipation model.

Figure 6.22: Critical density versus highway width for full, weak, and no nudging for driver's anticipation model.

Figure 6.23: Free flow speed versus highway width for full, weak, and no nudging for driver's anticipation model.

Figure 6.24: Capacity versus highway width for full, weak, and no nudging for driver's anticipation model.

Figure 6.25: Line graph representing the model's global parameter β based on the various highway widths and nudging scenarios (No nudging, Half nudging, and Full nudging).

Figure 6.26: Line graph representing the model's global parameter \tilde{v} based on the various highway widths and nudging scenarios (No nudging, Half nudging, and Full nudging).

Figure 6.27: Space-time diagrams of microscopically produced speed (ground truth) versus macroscopic model estimates (model) for highway width of 9.3 m and half nudging for the extended version of driver's anticipation model.

Figure 6.28: Space-time diagrams of microscopically produced flow (ground truth) versus macroscopic model estimates (model) for highway width of 9.3 m and half nudging for the extended version of driver's anticipation model.

Figure 6.29: Space-time diagrams of microscopically produced speed (ground truth) versus macroscopic model estimates (model) for highway width of 11.9 m and full nudging for the extended version of driver's anticipation model.

Figure 6.30: Space-time diagrams of microscopically produced flow (ground truth) versus macroscopic model estimates (model) for highway width of 11.9 m and full nudging for the extended version of driver's anticipation model.

Figure 6.31: Line graph representing the model's objective function values based on the various highway widths and nudging scenarios (No nudging, Half nudging, and Full nudging) for the extended version of driver's anticipation model.

Figure 6.32: Critical density versus highway width for full, weak, and no nudging for the extended version of driver's anticipation model.

Figure 6.33: Capacity versus highway width for full, weak, and no nudging for the extended version of driver's anticipation model.

Figure 6.34: Free flow speed versus highway width for full, weak, and no nudging for the extended version of driver's anticipation model.

Figure 6.35: Line graph representing the model's global parameter β_1 and β_2 based on the various highway widths and nudging scenarios (No nudging, Half nudging, and Full nudging).

Figure 6.36: Line graph representing the model's global parameter \tilde{v} based on the various highway widths and nudging scenarios (No nudging, Half nudging, and Full nudging).

Figure 6.37: Line graph representing the objective function values of the 4 models based on the various highway widths and no nudging scenario.

Figure 6.38: Line graph representing the objective function values of the 4 models based on the various highway widths and half nudging scenario.

Figure 6.39: Line graph representing the objective function values of the 4 models based on the various highway widths and full nudging scenario.

List of Tables

Table 5.1: *The different dimensions of vehicles used in the simulation experiment.*

Table 6.1: *The objective function values for each width and nudging scenario in the original CTM.*

Table 6.2: *The objective function values for each width and nudging scenario in the extended version of CTM.*

Table 6.3: *The objective function values for each width and nudging scenario in the driver's anticipation model.*

Table 6.4: *The objective function values for each width and nudging scenario in the extended version of driver's anticipation model.*

Chapter 1

Introduction

1.1 Motivation

A critical requirement in the realm of Intelligent Transportation Systems (ITS) is the effective modeling of traffic flow within large-scale freeway networks. ITS are advanced applications aimed at providing innovative services related to different modes of transport and traffic management. These systems enable users to be better informed and make safer, more coordinated, and smarter use of transport networks. The importance of ITS lies in their ability to significantly reduce traffic congestion, accident risks, and emergency situations by leveraging cognitive networking principles. This involves developing transportation management mechanisms with learning capabilities to perceive potential dangers in advance and adjust vehicle behavior accordingly. The application of ITS leads to improved efficiency and safety of mobility, reducing time losses, pollution, and energy waste, and enhancing the overall quality of life [1].

The continuously increasing number of vehicles utilizing the available network capacity has led to significant issues, manifesting as both recurrent and non-recurrent congestion. This congestion results in substantial economic and environmental challenges, along with heightened public frustration and discomfort. More specifically, traffic congestion leads to excessive delays, significant environmental pollution, and diminished traffic safety. In Europe, the annual cost of road traffic congestion exceeds €120 billion, not including the additional environmental pollution and traffic accident costs, the latter being approximately four times higher. Similar statistics are observed in the United States [2]. While conventional traffic management measures are beneficial, they are insufficient to mitigate the severe congestion conditions. A more comprehensive approach is required, one that leverages the progressively emerging and future groundbreaking capabilities of vehicles and infrastructure.

Over the past decade, substantial efforts by the automotive industry and numerous research institutions have focused on developing and deploying a variety of Vehicle Automation and Communication Systems (VACS) [3], promised to revolutionize the capabilities of individual vehicles. VACS are categorized into Vehicle Automation Systems (VAS), which range from basic driver support to fully automated driving, and Vehicle Communication Systems (VCS), which enable V2V (vehicle-to-vehicle) and

V2I (vehicle-to-infrastructure) communication [4]. Several low-automation VACS are already available on the market, such as Adaptive Cruise Control (ACC), which automatically adjusts the vehicle speed to the driver's selected desired speed or modulates the distance when a slower vehicle is detected ahead.

As we transition into the era of full automation, one potential solution is achieving 100% penetration of CAVs, utilizing essential movement strategies for both lateral and longitudinal directions. With the elimination of human drivers, road rules can be either relaxed or disregarded. CAVs hold the promise of enhancing safety, improving traffic flow, reducing emissions, and fostering economic development. However, due to the inherent complexity of vehicular traffic, sophisticated algorithms such as nonlinear feedback control and advanced artificial intelligence techniques like reinforcement learning are necessary to facilitate effective decision-making [5].

1.2 TrafficFluid

For future traffic comprising exclusively CAVs, an innovative concept known as TrafficFluid [6] has been proposed. The TrafficFluid paradigm is defined by two integrated principles: lane-free traffic and vehicle nudging. The principle of lane-free traffic eliminates the conventional requirement for vehicles to adhere to fixed lanes. Instead, vehicles operate in a lane-free environment, self-organizing into dynamically changing 2-D clusters [7]. This organization depends on factors such as vehicle sizes, desired speeds, employed movement strategies, and prevailing vehicle density, aiming to maximize the use of available infrastructure. The principle of nudging forces allows vehicles to be influenced by others in their vicinity, including those behind them. It is important to emphasize that the concept of nudging forces is inspired by the lane-based car-following principles of ACC law.

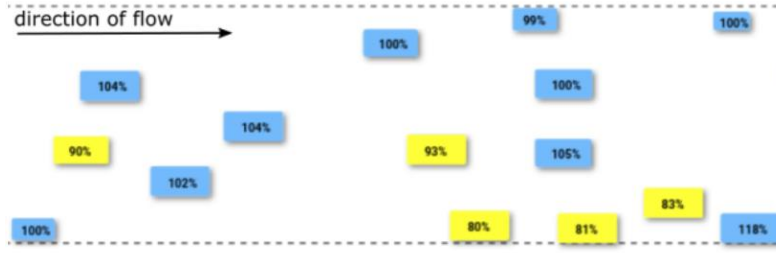


Figure 1.1: The layout of a lane-free highway.

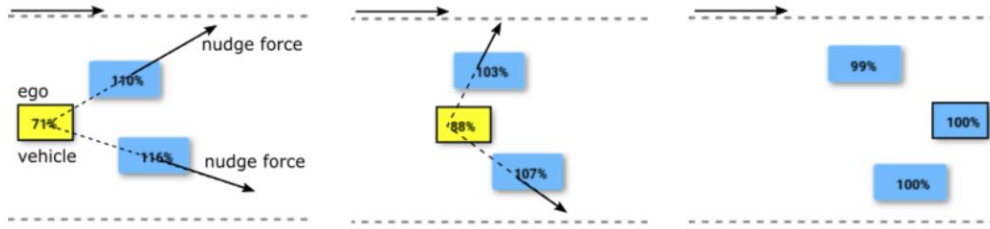


Figure 1.2: The principle of vehicle nudging.

1.3 Thesis Objectives

In this thesis, four first-order macroscopic models will be examined: the original Cell Transmission Model (CTM) [8], an Extended Version of CTM [7], the Drivers' Anticipation Model [9], and an Extended Version of the Drivers' Anticipation Model. These four macroscopic models were evaluated to a hypothetical freeway network, featuring an off-ramp and an on-ramp. The application of these models relies on data derived from microscopic simulations conducted within the TrafficFluid-Sim environment. In this environment, a comprehensive examination of eight different width configurations was conducted, with each width scenario evaluated under three distinct conditions: no nudging, half nudging, and full nudging. The calibration of the models was tailored to this specific network, requiring the estimation of optimal parameter values through the analysis of microscopic traffic data.

To accomplish this calibration, an innovative software tool named CALISTO was employed [10]. CALISTO was appropriately expanded to accommodate the intricacies of both the Drivers' Anticipation Model and its Extended Version.

The findings of this investigation were expected to yield satisfactory results, demonstrating that the macroscopic models will be capable of faithfully replicating

real-world conditions. It is anticipated that in most instances, both highway capacity and critical density will exhibit a linear correlation with increasing highway width. Additionally, further augmentation of these parameters was observed with heightened levels of vehicle nudging. Conversely, it is expected that the free flow speed will remain largely unaffected by variations in highway width, albeit showing a slight increment in tandem with increased levels of vehicle nudging.

1.4 Thesis Outlines

This diploma thesis is composed of six chapters. Chapter 2 explores the science of traffic flow from a microscopic perspective. In this chapter, the kinematic equations of vehicles are explained, along with the concept of nudging between vehicles.

Chapter 3 delves into the macroscopic aspects of traffic flow, presenting the fundamental diagram and the conservation equation. It also examines the mathematics underlying the CTM model, its extended version, the drivers' anticipation model, and the extended drivers' anticipation model. Moreover, this chapter includes explanations of the code components for the two latest models.

Chapter 4 introduces the software application CALISTO, detailing its basic components, including the calibration method and the Nelder-Mead optimization algorithm.

Chapter 5 delves into the implementation process, providing a detailed analysis. It describes the methodology used for conducting microscopic simulations and explains the calibration process carried out using CALISTO.

In Chapter 6, the results of the simulations for the four macroscopic models are presented, along with a comparative analysis of their performance.

Chapter 7 presents the conclusions and provides a brief overview of the approach and key findings of this diploma thesis.

Chapter 2

The Microscopic World

2.1 Vehicle Moving Strategy

Microscopic models depict the space-time dynamics of individual vehicles and their interactions with the surrounding traffic environment. This behavior is characterized by dynamic variables including position, velocity, and acceleration. While microscopic traffic flow models necessitate significant computational resources, they offer a mathematically precise traffic flow simulation [11].

Designing a vehicle movement strategy that ensures safety and efficiency in lane-free traffic poses a significant challenge. Numerous methodological approaches have been investigated to address this issue, encompassing strategies based on optimal control, non-linear feedback control, and multi-agent systems [7]. To illustrate and validate the TrafficFluid concept, an ad-hoc vehicle movement strategy for lane-free traffic, incorporating nudging vehicles, was developed. In Chapter 5, an exposition is provided on the inherent properties characterizing ad-hoc strategy and microscopic simulations.

The vehicle position and speed are described using the following two-dimensional kinematic dynamics:

$$x(t + T) = x(t) + v_x(t)T + 0.5f_x(t)T^2 \quad (2.1)$$

$$v_x(t + T) = u_x(t) + f_x(t)T \quad (2.2)$$

$$y(t + T) = y(t) + v_y(t)T + 0.5f_y(t)T^2 \quad (2.3)$$

$$v_y(t + T) = v_y(t) + f_y(t)T \quad (2.4)$$

At each time-step T , each vehicle initiates its motion from the position denoted by $(x(t), y(t))$, representing the longitudinal and lateral coordinates of its rectangular center. This positioning is accompanied by longitudinal speed $v_x(t)$ and lateral speed $v_y(t)$. Governed by constant longitudinal acceleration $f_x(t)$ and lateral acceleration $f_y(t)$, the vehicle progresses to its updated state, encompassing both position and velocity, at time $t + T$. It is imperative to note that in the equations, the acceleration serves as a controlled input, determined by the vehicle's motion strategy.

In the employed vehicle moving strategy, longitudinal and lateral accelerations for each CAV at time t are computed via the following equations:

$$f_x(t) = \sigma_x^{ts} f_x^{ts}(t) + f_x^{rp}(t) + \sigma^{ng} \gamma_x f_x^{ng}(t) \quad (2.5)$$

$$f_y(t) = f_y^{ts}(t) + f_y^{rp}(t) + \sigma^{ng} \gamma_y f_y^{ng}(t) \quad (2.6)$$

The numerical values of the accelerations $f_x(t)$ and $f_y(t)$ are determined by specific components along the x and y axes. These components include the target forces $f_x^{ts}(t)$ and $f_y^{ts}(t)$, the repulsive forces $f_x^{rp}(t)$ and $f_y^{rp}(t)$ and the nudging forces $f_x^{ng}(t)$ and $f_y^{ng}(t)$. A comprehensive description of these parameters will be provided in the Section 2.2 for a more analytical approach, please refer to [2]). The activation or the deactivation of the target-speed force $f_x^{ts}(t)$ is controlled by the binary variable $\sigma_x^{ts} \in \{0,1\}$. The nudging forces $f_x^{ng}(t)$ and $f_y^{ng}(t)$ can also be deactivated under certain conditions, controlled by the binary variable $\sigma^{ng} \in \{0,1\}$. The coefficients γ_x and γ_y , which range between 0 and 1, adjust the balance between nudging and repulsive forces, allowing for the increase or decrease of nudging forces if necessary.

2.2 Forces

The vehicle movement strategy employs an "artificial forces" methodology, wherein longitudinal and lateral forces dictate vehicle acceleration in two dimensions. Three distinct 2-D forces influence movement in both the longitudinal and lateral directions. Firstly, the target-speed force, which can be either positive, zero or negative, is determined by the difference between the vehicle's current speed and its desired speed; in the lateral direction, the desired speed is zero. Secondly, vehicles generate repulsive forces that diminish with distance and are applied to trailing vehicles to prevent collisions. Thirdly, vehicles produce nudging forces that also fade with distance and are

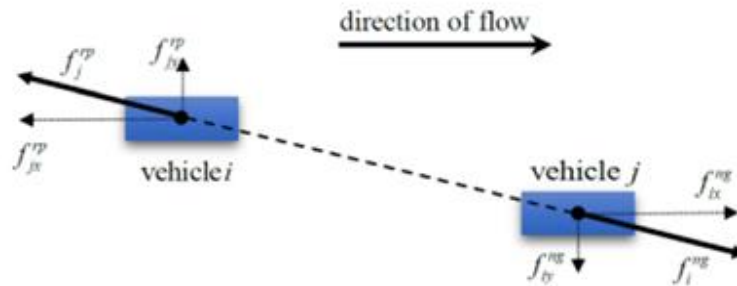


Figure 2.1: Visualization of repulsive and nudging forces between two vehicles.

exerted on vehicles ahead to maintain flow (see Figure 2.1). Weighting parameters are used to modulate the impact of each force. After computing these forces, a bounding mechanism may be employed to limit them before they are translated into vehicle accelerations. This bounding mechanism ensures adherence to various technical constraints, particularly maintaining compliance with lateral road boundaries.

2.2.1 Target - Speed Forces

Each vehicle has an associated target speed that is non-zero in the longitudinal direction v_x^d and zero in the lateral direction v_y^d . The force applied on a vehicle adjusts based on whether it is traveling below, at, or above its desired longitudinal or lateral speed. Specifically, the target force components f_x^{ts} (f_y^{ts}) become positive if the vehicle is moving below the target speed, zero if it is at the target speed, and negative if it is moving above the target speed. Thus, we have the following relations:

$$f_x^{ts}(t) = \text{erfc}[0.2(v_x(t) - v_x^d)] - 1 \quad (2.7)$$

$$f_y^{ts}(t) = \text{erfc}[0.5(v_y(t) - v_y^d)] - 1 \quad (2.8)$$

where the complementary error function is $\text{erfc}(x) = \frac{2}{\sqrt{\pi}} \int_x^\infty e^{-t^2} dt$.

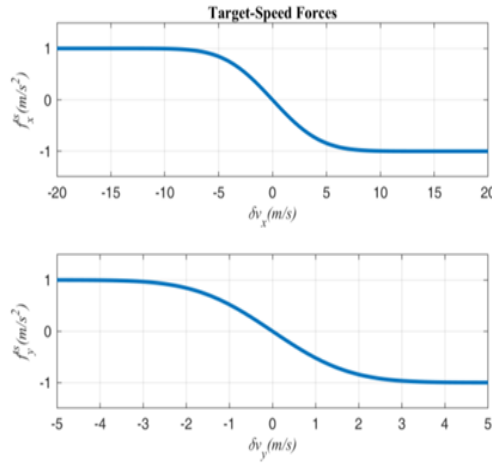


Figure 2.2: The target-speed forces providing deceleration or acceleration, as needed, to address deviations from a desired speed.

2.2.2 Repulsive and Nudging Forces

For each pair of adjacent vehicles i and j , a repulsive force is generated, directed along the line connecting the centers of both vehicles. This force acts upon the vehicle whose center is located further upstream.

$$\Pi(\Delta x, \Delta y, \Delta v_x, L_y, D_y) = F(\Delta x, \Delta v_x) H(\Delta y, L_y, D_y) \quad (2.9)$$

The function $F(\Delta x, \Delta v_x)$ is contingent upon longitudinal variables, notably the longitudinal distance $\Delta x = x_j - x_i$ and the longitudinal relative speed $\Delta v_x = v_{jx} - v_{ix}$ for vehicle i (follower) and j (leader vehicle). The function $F(\Delta x, \Delta v_x)$ is multiplied by a separate function that relies solely on lateral parameters, in the following manner.

$$H(\Delta y, L_y, D_y) = \max \left\{ 0, \min \left\{ 1, 1 - \frac{\Delta y - D_y}{L_y}, \frac{\Delta y + D_y + L_y}{L_y} \right\} \right\} \quad (2.10)$$

In the graphical depiction, the function's significance becomes evident. It is noted that the repulsion between vehicles is primarily crucial when both are longitudinally aligned, progressively diminishing to zero as the lateral displacement increases.

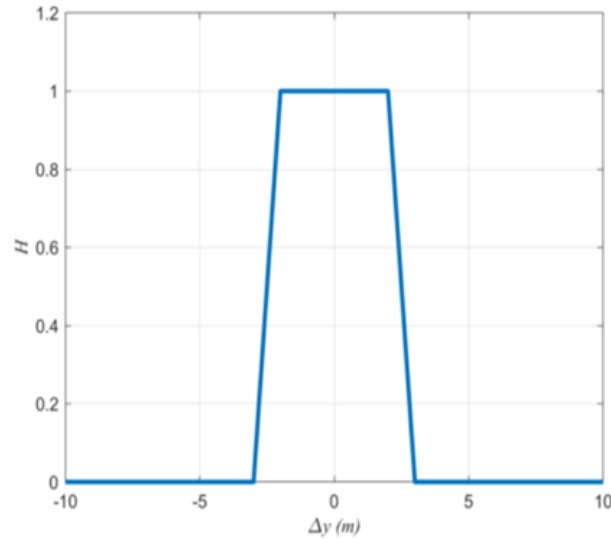


Figure 2.3: The graphical depiction of function $H(\Delta y, L_y, D_y)$.

The downstream vehicle j receives, due to the upstream vehicle i , a nudging force f_i^{ng} with a magnitude $|f_i^{ng}| = |f_i^{rp}|$. This equality, particularly depicted in Figure 2.1, adheres to Newton's Law of Action and Reaction. Nevertheless, the mathematical flexibility permits the adjustment of the nudging force magnitude through the coefficients γ_x and γ_y .

Let us now focus on the term $F(\Delta x, \Delta v_x)$. Figure 2.4 illustrates an Action Graph (AG) in $(\Delta x, \Delta v_x)$ coordinates, plotting the relative longitudinal speed Δv_x against the longitudinal distance Δx between the downstream vehicle j and the upstream vehicle i . The AG is segmented into distinct regions, each corresponding to specific actions based on the measured $(\Delta x, \Delta v_x)$ for the vehicle pair. These actions pertain to the follower, denoted as the vehicle whose center is positioned further upstream. For instance, if the leader exhibits a higher speed than the follower $\Delta v_x > 0$, no repulsion force is required, enabling the follower to accelerate towards its desired speed. Conversely, if the leader's speed is lower than that of the follower $\Delta v_x < 0$, the follower may need to decelerate. Three discrete areas are delineated: the no-repulsion area, where the follower endeavors to attain its desired speed; the deceleration area, where appropriate deceleration is initiated; and the emergency area, where full braking is engaged to prevent collisions (for a more detailed analysis, refer to [12]).

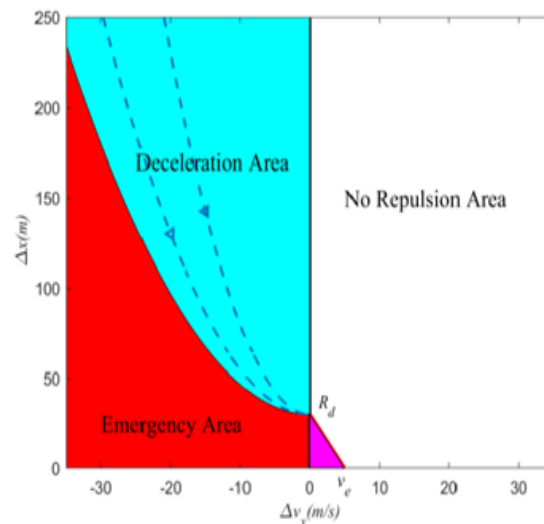


Figure 2.4: Action Graph depicting the acceleration strategy based on the longitudinal distance and relative speed between vehicles j and i .

Chapter 3

The Macroscopic World

3.1 Macroscopic vs. Microscopic Models

Macroscopic models in comparison with the microscopic ones represent traffic in a more aggregated manner, treating traffic flow as a fluid with distinct characteristics. The primary traffic variables used to describe the dynamics of this fluid are mean speed, density, and traffic flow (or volume). The macroscopic traffic flow models are classified into first-order, second-order, or higher-order models, depending on the number of differential equations they encompass [7].

This thesis will focus on employing first-order macroscopic models. Their analytical form makes them suitable for a range of critical traffic engineering applications, such as estimation [13] and control strategy design [14], beyond mere simulation. Additionally, macroscopic models can provide more direct insights into the characteristics of lane-free traffic with nudging, without high computational cost. A key expectation for the macroscopic model is its ability to accurately reproduce highway conditions and try to predict capacity drop phenomena. These phenomena primarily occur at bottleneck locations, which are areas characterized by specific infrastructure layouts such as lane reductions, tunnels, and similar features. Empirical data from highways with lanes indicate that when a bottleneck is activated, the maximum outflow decreases by 5 to 20% below the nominal capacity of the bottleneck [9].

Three of the four first-order macroscopic models employed in this thesis—the Extended Version of CTM model [7], the Drivers' Anticipation Model [9], and an Extended Version of the Drivers' Anticipation Model—can predict this capacity drop phenomenon effectively. But not as effectively as a second-order model (such as METANET [15]) can do.

3.2 Fundamental Diagram

The macroscopic description of traffic flow necessitates the definition of appropriate variables that capture the average behavior of vehicles at a specific location and time. We define traffic density, $\rho(x, t)$ as the number of vehicles per section length (veh/km). The space mean speed, $v(x, t)$ (km/h), represents the instantaneous average speed of vehicles over a length increment, (as described by Wardrop [16]). Traffic volume,

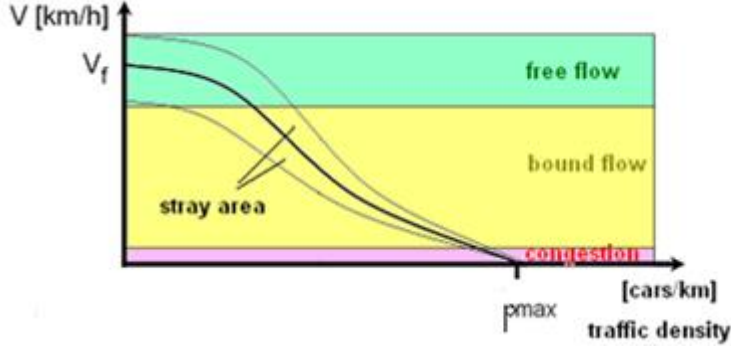


Figure 3.1: A general graphical representation of the relationship between speed and density.

$q(x, t)$ is defined as the number of vehicles passing a specific location within a unit of time (veh/h). From these definitions of variables, we derive the fundamental relationship between them,

$$q = \rho \cdot v \quad (3.1)$$

To ensure safety, the spacing between vehicles is adjusted according to their velocities, and similarly, velocities adapt based on vehicle spacing. This means that as traffic density increases along a section of the freeway—resulting in shorter gaps between vehicles—the average speed naturally decreases. Various mathematical models have been developed to describe the relationship between speed and density under uniform conditions. One commonly used general formula for velocity as a function of density, $v(p)$, satisfies the relevant boundary conditions and is expressed as follows:

$$v(p) = v_f \left(1 - \left(\frac{\rho}{\rho_{jam}}\right)^l\right)^m \quad (3.2)$$

where $l, m > 0$

There are variations of the speed equation such as:

$$v(\rho) = v_f \cdot e^{\left(\frac{1}{a} \left(\frac{\rho}{\rho_{cr}}\right)^a\right)} \quad (3.3)$$

as well as a polynomial equation,

$$v(\rho) = \sum_{i=0}^p \alpha_i \cdot \rho^i \quad (3.4)$$

where $\alpha_i, i = 0, \dots, p$, are constant parameters (for further analysis, see [17]).

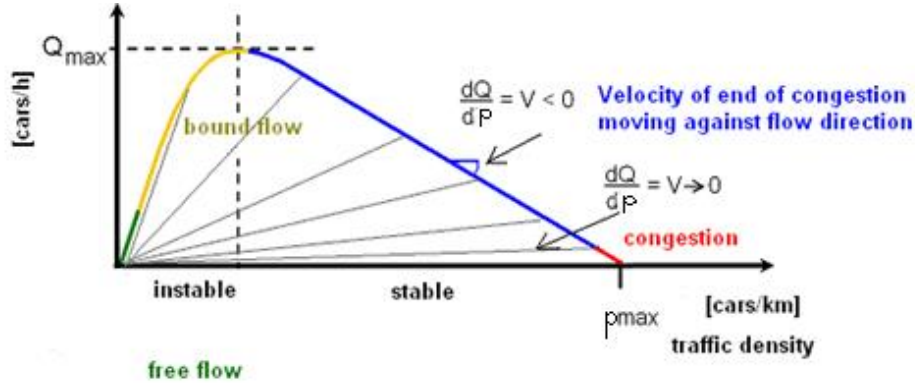


Figure 3.2: A general graphical representation of the relationship between flow and density.

By substituting $v(\rho)$ into equation 3.1, we derive a volume-density relationship $Q(\rho)$, which is commonly referred to as the fundamental diagram (FD) in traffic engineering.

$$Q(\rho) = \rho \cdot v(\rho) \quad (3.5)$$

The Figure 3.2 shows the FD. It clearly demonstrates that the relationship between flow (Q) and density (ρ) is nonlinear. It is important to highlight that this nonlinear characteristic with a slightly different shape is consistent in both the driver's anticipation model and its extended form. At this point, we need to clarify that the flow-density relationship can exhibit both nonlinear and linear characteristics (such as in the CTM model), depending on the specific requirements and assumptions of the model being utilized. Observing this figure, we can also conclude that initially, a positive correlation exists between traffic density and flow rate. However, this relationship reaches a critical point, beyond which a further increase in density leads to a decline in flow rate, signifying after a while the onset of congestion. When the system operates at critical density (ρ_{cr}), it achieves maximum flow.

3.3 LWR Model

The Lighthill-Whitham-Richards (LWR) model [19] is a cornerstone of traffic flow theory, providing a mathematical framework to describe the evolution of traffic density on highways over time. This model is grounded in three fundamental principles:

1. **Conservation of Vehicles:** The model assumes no changes in the number of vehicles on the road, implying that there are no on-ramps or off-ramps.
2. **Conservation of Flow:** The model adheres to the principle of matter conservation, ensuring that the flow of vehicles is balanced.
3. **Propagation of Density Waves:** The model accounts for the propagation of traffic density waves along the highway.

These principles are encapsulated in the following partial differential equation:

$$\frac{\partial \rho}{\partial t} + \frac{\partial Q}{\partial x} = 0 \quad (3.6)$$

The equation ensures that vehicles are neither created nor destroyed. If the density of vehicles is increasing at a point (positive $\frac{\partial \rho}{\partial t}$), it must be because vehicles are flowing into that point faster than they are leaving (negative $\frac{\partial Q}{\partial x}$). While the LWR model provides a robust framework for understanding basic traffic flow dynamics, its simplifications, such as the assumption of a continuous and homogeneous traffic stream, limit its effectiveness in more complex scenarios. Therefore, to address real-world complexities such as varying road geometries and traffic behaviors, several advanced models have been developed, extending the basic principles of the LWR model.

Authors in [18] presented a differential equation to model traffic flow on a long, multi-lane highway with numerous on-ramps and off-ramps. The focus is on developing mathematical models that describe the dynamic evolution of traffic variables along the highway. By treating traffic flow as a fluid characterized by density $\rho(x, t)$ and flow $q(x, t)$, the fundamental equation of conservation of matter can be written as follows:

$$\frac{\partial \rho}{\partial t} + \frac{\partial Q}{\partial x} = r - s \quad (3.7)$$

In this context, $r - s$ represents the exogenous source term accounting for on-ramps and off-ramps.

Also, in real-world conditions, traffic often experiences sudden changes in density, such as the formation of traffic jams, which are better described by the concept of shock waves. To model these shock waves, the following equation can be used:

$$\frac{dX_s}{dt} = \frac{Q(\rho_2) - Q(\rho_1)}{\rho_2 - \rho_1} \quad (3.8)$$

Here, $\frac{dX_s}{dt}$ represents the speed at which the discontinuity (shock wave) travels along the freeway. $Q(\rho)$ denotes the traffic volume as a function of traffic density ρ , with ρ_1 and ρ_2 representing the densities on either side of the shock wave. This equation highlights how the speed of the shock wave depends on the difference in traffic flow between the two regions with different densities. It provides insights into the dynamics of traffic jams and their propagation, an area where the LWR model's basic assumptions may fall short.

However, for the needs of this thesis, it is more practical to use discrete time-steps in equations. To achieve this, we divide the freeway into N sections, each with a length L_i for $i = 1, \dots, N$. In real-world scenarios, the delineation of a new section occurs when there are changes in the freeway's geometry, such as the addition of an on-ramp or the removal of a lane. Thus, each section can contain at most one on-ramp and one off-ramp. A more in-depth exploration of the discrete model's application is provided in Section 3.4, where the CTM model is comprehensively presented.

3.4 Original CTM and Extended Version

Cell Transmission Model (CTM) is a discrete-time, discrete-space model for traffic flow that approximates the continuous LWR model. It is well-known that the original CTM does not replicate the capacity drop phenomenon observed in real traffic, where flow rates at congestion heads are lower than the freeway theoretical capacity. This discrepancy in conventional traffic is attributed to the constrained and varied acceleration capabilities among different vehicles (see [20]).

To address this limitation, CTM has undergone several extensions to more accurately capture the capacity drop phenomenon. In this section, we first delve into the mathematical formulation of the original CTM, highlighting its inability to model the capacity drop. Subsequently, we introduce an enhanced version of CTM that incorporates additional mechanisms to simulate this phenomenon more effectively.

Original CTM

The conservation equation for each section is given by:

$$\rho_1(t+1) = \rho_1(t) + \frac{T}{L_1}(q_o(t) - q_1(t)) \quad (3.9)$$

$$\rho_i(t+T) = \rho_i(t) + \frac{T}{L_i}((1-s_i(t))q_{i-1}(t) - q_i(t) + r_i(t))$$

$$\text{for } i = 2, \dots, n \quad (3.10)$$

where $\rho_i(t)$ is the density in section i , T is the model time step, q_i is the mainstream flow of section i , $r_i(t)$ is the flow from an on-ramp at section i , $s_i(t)$ denotes the exit rate of an off-ramp, L_i is the length of section i and l_i is the number of lanes at section i .

The flow from section i to section $i+1$ is described by the following equations:

$$q_i(t) = \min \left\{ Q_{D,i}(\rho_i(t)), \frac{Q_{S+1}(\rho_{i+1}(t))}{(1-s_{i+1})} - r_{i+1}(t) \right\}$$

$$\text{for } i = 1, \dots, n-1 \quad (3.11)$$

$$q_n(t) = Q_{D,i}(\rho_n(t)) \quad (3.12)$$

where $Q_{D,i}$ (veh/h) is the demand part of the FD of the section i during $(t, t+1]T$, $Q_{S,i}$ (veh/h) is the supply part of the FD of the section i during $(t, t+1]T$.

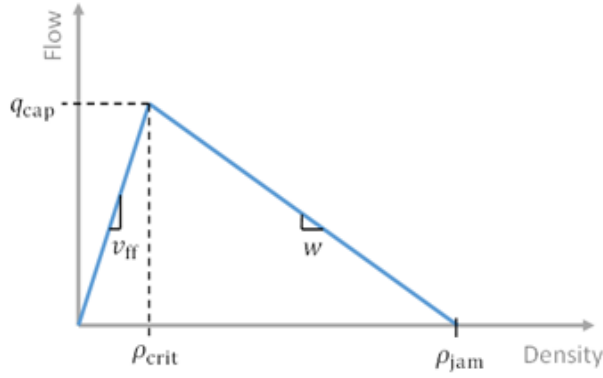


Figure 3.3: The triangular FD of original CTM.

The demand and the supply functions are as follows:

$$Q_{D,i}(\rho_i(t)) = \min\{q_{cap,i}, v_{f,i}\rho\}$$

$$\text{for } i = 1, \dots, n \quad (3.13)$$

$$Q_{S,i}(\rho) = \min\{q_{cap,i}, w_{s,i}(\rho_{max,i} - \rho)\}$$

$$\text{for } i = 1, \dots, n - 1 \quad (3.14)$$

where $v_{f,i}$ (km/h) is the free flow speed, $q_{cap,i}$ is the capacity flow of the section i , $w_{s,i}$ signifies the back-wave speed in km/h and $\rho_{max,i}$ (veh/km) indicates the storage density at the section i .

Extended Version of CTM

Over time, CTM has undergone various extensions aimed at effectively replicating the capacity drop phenomenon observed in real traffic scenarios. This thesis explains an enhanced version of CTM specifically designed to accurately model and reproduce the capacity drop phenomenon. The conservation equation of this extended version of CTM for each section is given by:

$$\rho_1(t+1) = \rho_1(t) + \frac{T}{L_1}(q_o(t) - q_1(t)) \quad (3.15)$$

$$\rho_i(t+T) = \rho_i(t) + \frac{T}{L_i}((1-s_i(t))q_{i-1}(t) - q_i(t) + r_i(t)) \quad (3.16)$$

The movement of vehicles between adjacent sections adheres to the steady-state relationship described by the FD (Figure 3.3), which as mentioned before relates flow to density. In this model, the traffic flow from a section i to a section $i+1$ is determined as the minimum of the demand function Q_D and the supply function Q_S as we can see in Equation (3.17), except for the final section where only the demand function is considered – Equation (3.18). This assumption is made under the condition that downstream traffic conditions remain uncongested. Specifically,

$$q_i(t) = \min \left\{ Q_{D,i}(\rho_i(t)), \frac{Q_{S,i+1}(\rho_{i+1}(t))}{(1-s_{i+1})} - \lambda_r r_{i+1}(t) \right\}$$

$$\text{for } i = 1, \dots, n-1 \quad (3.17)$$

$$q_n(t) = Q_{D,n}(\rho_n(t)) \quad (3.18)$$

The demand and supply functions are given by the following respective equations:

$$Q_{D,i}(\rho) = \min \left\{ q_{cap,i} + \lambda_d q_{cap,i} \frac{\rho - \rho_{cr,i}}{\rho_{cr,i} - \rho_{max,i}}, v_{f,i} \rho \right\} \quad (3.19)$$

$$Q_{S,i}(\rho) = \min \{ q_{cap,i}, w_{s,i}(\rho_{max,i} - \rho) \} \quad (3.20)$$

where v_f (km/h) represents the free-flow speed of section i , $q_{cap,i}$ (veh/h) denotes the section capacity achieved at critical density $\rho_{cr,i}$, $w_{s,i}$ signifies the back-wave speed in km/h, and $\rho_{max,i}$ (veh/km) indicates the jam density in vehicles.

To investigate the potential impact of capacity drop, we have integrated into the equations of the original CTM the capability to introduce this phenomenon. This enhancement is facilitated in this extended version through the global parameters λ_r and λ_d within the equations mentioned above. Setting the values for $\lambda_r = 1$ (which determines the proportion of on-ramp flow) and $\lambda_d = 0$ (which determines the proportion of mainstream flow) replicates the absence of capacity drop, consistent with

the original CTM approach. However, adjusting these parameters to values between 0 and 1 enables the model to simulate varying degrees of capacity drop. This modification allows for a more nuanced exploration of traffic dynamics, particularly in scenarios where congestion may occur, influencing both inflow and outflow rates accordingly.

3.5 First Order Model with Driver's Anticipation

The first-order traffic flow model with drivers' anticipation builds upon the foundational LWR model. This model diverges from the traditional LWR and CTM framework, which primarily employs a demand-supply methodology. Instead, it emphasizes the anticipatory behavior of drivers, leading to accurate traffic condition predictions. A key element of the model is the anticipation term, which quantifies the extent to which drivers anticipate future traffic conditions. This term plays a crucial role in enhancing the model's predictive capabilities. The anticipation-based model demonstrates a marked improvement in the prediction of traffic conditions compared to traditional first-order models such as the LWR model. It accurately simulates the propagation of congestion waves. However, its ability to depict the capacity drop phenomenon—where the actual outflow is lower than the theoretical capacity at bottlenecks—requires further enhancement. Before we project our expectations onto the model and identify its weaknesses, let's carefully examine its mathematical foundations.

First, we have the equation that represents the actual flow from section i to section $i + 1$:

$$q_i(\rho_i(t), \rho_{i+1}(t), \rho_{i+2}(t)) = \beta(1 - s_i)Q_i(\rho_i(t), \rho_{i+1}(t)) + (1 - \beta)(Q_{i+1}(\rho_{i+1}, \rho_{i+2}) - r_{i+1}(t))$$

for $i = 1, \dots, n - 2$ (3.21)

$$q_{n-1}(\rho_{n-1}(t), \rho_n(t)) = (1 - s_{n-1})Q_{n-1}(\rho_{n-1}(t), \rho_n(t))$$
(3.22)

$$q_n(\rho_n(t)) = g(\rho_n(t))$$
(3.23)

where:

- ρ_i is the density in section i .
- q_i denotes the actual outflow from the section i .

- $0 < \beta \leq 1$ is a model parameter adjusting the influence of anticipation.
- s_i and r_i refer to the on-ramp, off-ramp flows of section i .

As we can see, the flow function between sections exhibits three distinct boundary cases. For sections up to the second-to-last one, the equation incorporates Q_{i+1} term, which includes ρ_{i+2} as an argument, thereby accounting for density two sections ahead. In the second-to-last section, the Q_{i+1} term is omitted, while in the last section, the flow is determined solely by the fundamental diagram demand. In addition, we have the equation that represents the outflow from section i considering the FD of the specific section and the anticipation of driver's according to the downstream traffic flow conditions as:

$$Q_i(\rho_i(t), \rho_{i+1}(t)) = g(\rho_i(t)) - \frac{\tilde{v}l_i}{L_i}(\rho_{i+1}(t) - \rho_i(t)) \quad (3.24)$$

where:

- $g(\rho_i(t))$ represents the FD of the section i .
- \tilde{v} is a model parameter.
- l_i is the number of lanes.
- L_i refers to the length of section i .

As demonstrated in this paper [9], first-order LWR-type models with nonlinear FDs are employed in subsequent investigations of capacity drop approaches. Therefore, in this model, the fundamental diagram $g(\rho_i)$ is nonlinear, specifically defined as an exponentially increasing function,

$$g(\rho_i) = v_{f,i}\rho_i l_i e^{(-\frac{1}{c_i}(\frac{\rho_i}{\rho_{cr,i}})^{c_i})} \quad (3.25)$$

- $v_{f,i}\rho_i l_i$: Represents the maximum flow achievable at density ρ_i in section i .
- $e^{(-\frac{1}{c_i}(\frac{\rho_i}{\rho_{cr,i}})^{c_i})}$: Modulates the flow based on the density relative to ρ_{cr} . This term ensures that as ρ_i approaches and passes numerically ρ_{cr} , the flow decreases exponentially.

$$\text{where } c_i = \frac{-1}{\ln(\frac{q}{l_i v_{f,i} \rho_{cr,i}})} \quad (3.26)$$

Finally, the equations used to calculate the density and speed within each section are as follows:

$$\rho_i(t + T) = \rho_i(t) + \frac{T}{L_i} ((1 - s_i(t))q_{i-1}(t) - q_i(t) + r_i(t)) \quad (3.27)$$

$$v_i = \frac{q_i}{\rho_i} \quad (3.28)$$

Following the derivation of the governing equations that define the model, a graphical representation will be presented to illustrate the interactions within the model. In Figure 3.4, it can be observed how the model incorporating drivers' anticipation determines the actual flow from section i to section $i + 1$. The circles denote the sections into which the highway is divided. Let's say that the model tries to find the q_i . At this case, the model considers not only the density in i and $i + 1$ but also in section $i + 2$.



Figure 3.4: The illustration of the actual flow from section i to section $i + 1$ at drivers' anticipation model.

3.5.1 Explanation of Code for the Model with Driver's Anticipation in C++

Initialization of Model Parameters

This code is an integral part of the CALISTO software which CALISTO has been designed for the calibration procedure. The initial phase of the code involves setting up various parameters and vectors essential for simulating traffic flow with driver anticipation. Temporary vectors are created to represent the free-flow speed, critical density, and capacity flow for each link. All model parameters are consolidated into a single vector, which includes global parameters (β and \tilde{v}) as well as parameters specific to each Fundamental Diagram (FD) group. A mapping table is populated to link FD groups with their respective links and sections. Traffic state variables such as flow and speed are initialized for each section based on initial traffic data.

Re-initialization for Optimization

In the optimization phase, the model parameters are updated based on optimized values. This step is crucial for calibration, ensuring that the parameters reflect the latest optimized values. It involves updating both global parameters and FD group-specific parameters and recalculating the temporary vectors for free-flow speed, critical density, and flow capacity accordingly.

Clearing and Preparing Vectors

The code also contains a function that clears all vectors related to the model's parameters and state variables.

Main Simulation Loop

The main function is the core of the simulation, containing the main loop that iterates through the simulation steps to update traffic state variables. Firstly, it calculates the c_i term (Equation 3.26), which is used to determine the flow based on the fundamental diagram. After computing the c_i term for each section, the code calculates the value of the FD function for each section g_i (Equation 3.25), as well as the outflow for each section Q_i (Equation (3.24)). Additionally, the code computes the actual outflow q_i from section to section, ensuring a realistic representation of traffic flow across the network

(Equations 3.21, 3.22 and 3.23). At each iteration, the function updates the traffic density, actual flow, and velocity for each section. This process ensures that the model accurately reflects the evolving traffic conditions in each section of the network.

3.6 Extended Version of the Drivers' Anticipation Model

To enhance the effectiveness of the first-order model with driver's anticipation in accurately replicating real-world data, we propose an extension to the model by introducing an additional term β_2 . This term incorporates further information into the model, as the function for calculating the actual flow from section i to section $i + 1$, now also considers the density from the upstream section as well.

The revised formulation of the function, which accurately models the flow between sections, is presented as follows:

$$\begin{aligned}
 q_i(\rho_{i-1}(t), \rho_i(t), \rho_{i+1}(t), \rho_{i+2}(t)) \\
 = \beta_1 Q_{i-1}(\rho_{i-1}(t), \rho_i(t)) + (1 - \beta_1 - \beta_2)(1 - s_i) Q_i(\rho_i(t), \rho_{i+1}(t)) \\
 + \beta_2 (Q_{i+1}(\rho_{i+1}(t), \rho_{i+2}(t)) - r_{i+1}(t))
 \end{aligned}$$

for $i = 2, \dots, n - 2$ (3.29)

It should be noted that this relationship requires adjustments depending on the sections involved. Specifically, in the first section, the term q_{i-1} equals zero because it has arguments $\rho_{i-1}(t)$ and $\rho_i(t)$, with $\rho_{i-1}(t)$ not existing,

$$\begin{aligned}
 q_1(\rho_1(t), \rho_2(t), \rho_3(t)) &= (1 - \beta_2)(1 - s_1) Q_1(\rho_1(t), \rho_2(t)) + \beta_2 (Q_2(\rho_2(t), \rho_3(t)) - r_2(t))
 \end{aligned}$$

(3.30)

Following the same logic, the function for the second-to-last section cannot include the term q_{i+1} since the definition of the argument $\rho_{i+2}(t)$ cannot be established.

$$\begin{aligned}
 q_{n-1}(\rho_{n-2}(t), \rho_{n-1}(t), \rho_n(t)) \\
 = \beta_1 Q_{n-2}(\rho_{n-2}(t), \rho_{n-1}(t)) + (1 - \beta_1)(1 - s_{n-1}) Q_{n-1}(\rho_{n-1}(t), \rho_n(t))
 \end{aligned}$$

(3.31)

In the final section, it is established that the flow is solely determined by the fundamental diagram (FD).

$$q_n(\rho_n(t)) = g(\rho_n(t)) \quad (3.32)$$

The remaining equations ($c_i, g(\rho_i), Q_i$ and $\rho_i(t + T)$) adhere closely to the original model incorporating driver anticipation. To visualize the modification made to the original model, the key difference is that the updated model now incorporates and the upstream density (ρ_{i-1}) when it calculates the actual flow from section i to section $i + 1$.

The extended version of drivers' anticipation model achieves improved results primarily due to its enhanced ability to capture and simulate complex traffic dynamics more accurately than the original model. The extension model introduces an additional term in the flow calculation between sections, specifically incorporating the density of the upstream section. This adjustment allows the model to more realistically account for the influence of upstream traffic conditions on downstream flow, leading to a more precise representation of congestion propagation and release. Simply put, if the extended model fails to yield satisfactory results, the optimizer has the capability to reset the term q_{i-1} to zero, thereby reverting to the original model.



Figure 3.5: The illustration of the actual flow from section i to section $i + 1$ at the extended version of drivers' anticipation model.

3.6.1 Explanation of the Code for the Extended Version of the Drivers' Anticipation Model in C++

The extended version of the Driver's Anticipation Model builds on the same core structure as the original Driver's Anticipation Model in the CALISTO software, with key enhancements to capture more nuanced driver behaviors. The primary addition is a new global parameter, β_2 , which, alongside existing parameters like β_1 and \tilde{v} allows the model to more accurately simulate how drivers anticipate and respond to traffic conditions. These parameters are integral to adjusting the traffic flow and density calculations dynamically across different sections of the traffic network.

In this extended model, the main simulation loop is crucial for incorporating driver anticipation. Within this main function, traffic density, flow, and velocity for each section are updated iteratively. The new global parameter β_2 plays a significant role in the equations governing the actual outflow from section i to section $i + 1$, with its influence varying based on the section's position within the network. This model leads to a more refined calculation of outflows and inflows between sections.

Chapter 4

Traffic Flow Model Calibration

4.1 Calibration Procedure

The objective of the parameter estimation, or calibration, process is to enable a macroscopic traffic flow model to accurately represent the traffic conditions on a highway. Estimating the unknown parameters of the model is a challenging task due to the highly nonlinear nature of the system equations, which are nonlinear in both the parameters and the state variables. Consider a macroscopic discrete-time state-space model described by the following state equations,

$$\begin{aligned} x(t+1) &= f[x(t), d(t), p] \\ \text{for } t &= 0, 1, T-1 \end{aligned} \quad (4.1)$$

where x stands for the state vector, d is the external vector and p is the parameter vector, that needs to be specified. Specifically, the state vector x encompasses the section densities, the external variable vector d comprises the mainstream and on-ramp inflows as well as the turning rates at the off-ramps, and p contains the unknown model parameters that need to be determined.

In the context of traffic flow analysis, when a traffic project is initiated, data regarding the initial state and the external vector over a specified time horizon is typically provided. Consequently, the parameter estimation challenge can be framed as a nonlinear least-squares output error problem. This approach seeks to minimize the discrepancy between the model's predictions and the observed traffic data by employing the following cost function,

$$J(p) = \sqrt{\frac{1}{T} \sum_{t=0}^{T-1} [y(t) - y^m(t)]^2} \quad (4.2)$$

where $y(t) = g[x(t)]$ is the measurable model output vector (typically consisting of flows and mean speeds at various network locations) and $y^m(t)$ includes the measured traffic data (consisting of flows and speeds at corresponding network locations). The initial solution of the simplex, which we determine, significantly influences the

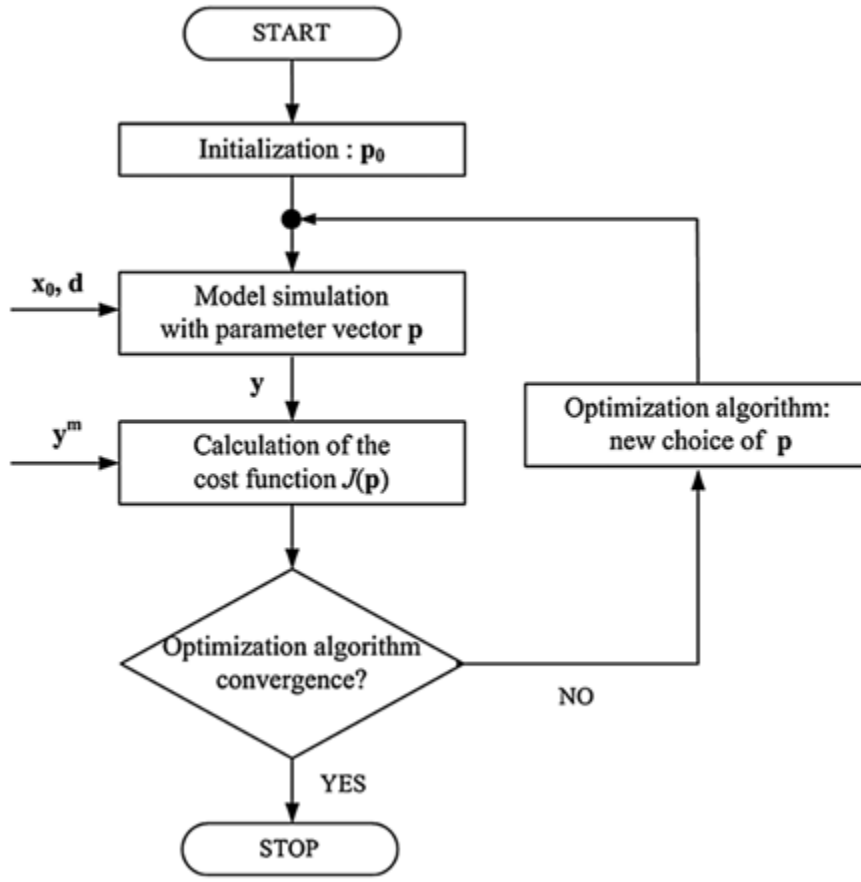


Figure 4.1: Flow chart describing how the calibration procedure works.

accuracy and convergence speed of the algorithm. The values of the model parameters are established based on physical considerations and prior experience.

The identification of the optimal set of parameters should be carried out using an appropriate programming loop routine. For each new parameter vector p , the value of the performance index can be computed through a calibration run, as describes the Figure 4.1.

The utilized performance index is given by the following relation,

$$J(p) = w_f \cdot RMSE_{flows} + w_s \cdot RMSE_{speeds} \quad (4.3)$$

where $RMSE_{flows}$ and $RMSE_{speeds}$ represents the root mean squared errors between the actual flow and speed measurements and the corresponding estimates generated by

the model. The terms w_f , w_s are the corresponding error weights for flow and speeds respectively.

In addition to the performance index, an optimization algorithm is required to determine the optimal set of values for the variables within the vector p . The nonlinear, non-convex least-squares optimization problem associated with parameter calibration is known to possess multiple local minima (see [21]), rendering gradient-based optimization algorithms unsuitable. Previous calibration studies have utilized various derivative-free optimization algorithms to address the parameter estimation problem, often without detailed analysis of their specific properties for the problem at hand.

Amidst the uncertainty regarding which algorithm is best suited to address the issue of multiple local minima, this paper [22] provides a definitive answer. The Nelder-Mead algorithm [23] utilizes a simplex, with each vertex representing a potential solution and its corresponding cost function value. The algorithm begins with an initial simplex and executes a series of transformations to minimize the highest cost function value among the vertices. These transformations are governed by four parameters: ζ for reflection, χ for contraction, γ for expansion, and σ for shrinkage.

In two words, the calibration procedure operates initially through the Nelder-Mead algorithm, which seeks to identify optimal pairs of values for the variables under consideration. For each pair identified by the algorithm, the deviation between the observed data and the calculated values is assessed using the cost function. If the resulting deviations are not satisfactory, this iterative process is repeated until convergence is achieved or the termination criteria are met. The termination criteria for the calibration procedure are defined as follows: the termination tolerance on the performance index value, the termination tolerance on the parameter vector values, and the maximum number of iterations allowed.

4.2 Nelder Mead Algorithm

The Nelder-Mead algorithm [23] is a heuristic search method used for finding the minimum of a function in a multidimensional space. It operates on a simplex, a geometric figure with $n + 1$ vertices in n -dimensional space (e.g., a triangle in 2D space). The algorithm iteratively updates the simplex vertices to converge towards the function's minimum.

The Nelder-Mead algorithm is a derivative-free optimization technique well-suited for solving nonlinear problems characterized by multiple local minima. This method is particularly effective for unconstrained optimization tasks. It operates using a simplex, an n -dimensional geometric shape with $n + 1$ vertices. Each vertex (where $i = 1, 2, \dots, n + 1$) represents a potential solution and corresponds to a specific value of the objective function, denoted as $J(p_i)$.

The algorithm begins with an initial simplex and iteratively applies a series of geometric transformations aimed at decreasing the objective function values at the vertices. The choice of the initial simplex is crucial, as it significantly influences the algorithm's performance and the accuracy of the solution. Through these transformations, the simplex adapts and converges towards an optimal solution, minimizing the objective function value.

The steps of the algorithm are mainly four. These are the reflection, the expansion, the contraction and the shrink with their parameters. More specifically, the simplex transformations in the Nelder-Mead are controlled by:

- ζ : Reflection coefficient, typically $\zeta = 1$.
- χ : Contraction coefficient, typically $\chi = 1$.
- γ : Expansion coefficient, typically $\gamma = 2$.
- σ : Shrink coefficient, typically $\sigma = 0.5$.

To gain a deeper understanding of the operational mechanics of this algorithm, it is essential to explore the various transformations applied to the simplex.

Reflection: The purpose of reflection is to explore a new point by reflecting the worst vertex across the centroid of the remaining vertices.

1. Calculation of the Centroid (CEN): The centroid is the average of all vertices of the simplex except the worst vertex (W).

$$CEN = \frac{1}{n} \sum_{i=1}^n x_i \quad (4.4)$$

2. The reflected point R is computed as:

$$R = CEN + \zeta(CEN - W) \quad (4.5)$$

3. Evaluation: The function value at R is evaluated. If this value is better than that at point W but not better than the best vertex, the worst vertex W is replaced by R .

Expansion: The purpose of this kind of transformation is to explore further the promising direction indicated by the reflection if the reflected point is particularly good.

1. Expansion Point (E): If the reflection R is better than the best simplex's point, then I calculate the expansion point E as:

$$E = CEN + \gamma(CEN - W) \quad (4.6)$$

2. Replacement: If the value E is better than R , then W is replaced by E . Otherwise, W is replaced by R .

Contraction: If the reflected point is not satisfactory, then I apply contraction which means the reduce of the simplex size to explore closer to the centroid.

1. Outside Contraction: If R is not better than any other point except W , the algorithm performs this kind of contraction,

$$C = CEN + \chi(CEN - W) \quad (4.7)$$

2. Inside Contraction: If R is worse than W , an inside contraction is performed,

$$C = CEN - \chi(CEN - W) \quad (4.8)$$

3. Replacement: If the contraction point C is better than W , the W is replaced by C . Otherwise, the algorithm proceeds to the shrink step.

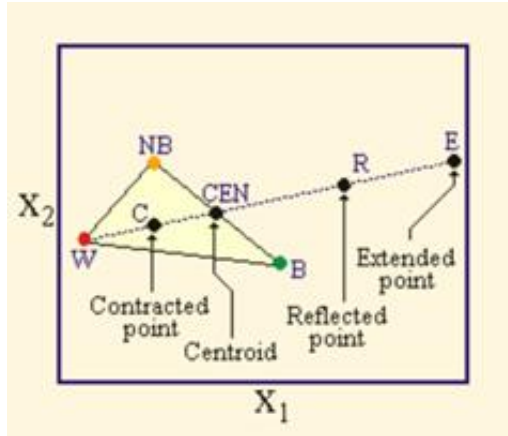


Figure 4.2: The graphical representation of the simplex, illustrating the available transformations within the algorithm, includes reflection, contraction, expansion, and shrink.

Shrink: It's the step where the algorithm reduces the size of the simplex because contraction has failed to improve the situation.

1. Shrink the Simplex: All the vertices except the best one are moved towards the best vertex,

$$x_i = x_{best} + \sigma(x_i - x_{best}) \quad (4.9)$$

By applying these transformations iteratively, the Nelder-Mead algorithm adapts the shape and size of the simplex to efficiently converge towards the minimum of the objective function.

4.3 CALISTO Software Tool

The previously developed CALISTO [24] is a software application designed to calibrate and verify macroscopic traffic flow models using real traffic data from various freeway sites. For the purposes of this study, CALISTO has been extended to accommodate the first-order model incorporating drivers' anticipation, along with its extended version. Specifically, the functionalities of the two drivers' anticipation model, as delineated in Sections 3.5, 3.6, have been integrated into the software. This section provides a concise overview of the enhanced CALISTO tool.

4.3.1 CALISTO Interface Window

The features of CALISTO encompass several critical aspects necessary for its operation. The description of the **freeway network** includes all the essential information to characterize the freeway site being analyzed, such as the number of mainstream sections, on-ramps and off-ramps and its locations, the number of detectors and lanes at the entrance and at the exit. The **traffic data feature** encompasses details pertinent to the simulated traffic data, such as the measurement interval, the simulation duration, and the location of the input file containing real traffic data.

Additionally, the tool includes various **other settings**, which cover the simulation step and additional features related to the performance index utilized and the simulation outputs. Users can select one of the available **traffic flow models** (CTM, METANET etc.) and specify the corresponding model parameter values. Furthermore, the tool uses the **optimization algorithm** Nelder-Mead to calibrate the chosen traffic flow model.

The software provides two operational modes: **Calibration** and **Validation**. After selecting the desired operation, the execution phase runs the selected operation, considering all the provided information. This structured approach ensures comprehensive calibration and validation of traffic flow models, enhancing the tool's utility in analyzing freeway traffic.



Figure 4.3: The window's interface of CALISTO.

Chapter 5

Implementation

5.1 Microscopic Simulation Set up and Traffic Data

After formalizing the ad-hoc movement strategy, it is essential to assess whether the theoretical framework aligns with practical reality. For this reason, a series of detailed microscopic simulations, each one lasting 1 hour of simulation time, were conducted using the ad-hoc vehicle movement strategy presented in Section 2.1. These simulations were conducted within the TrafficFluid-Sim framework (learn for TrafficFluid-Sim at [25],[26]) to generate the macroscopic traffic data essential for calibrating macroscopic traffic flow models. The vehicle movement strategy was applied with a time step of 0.2 seconds on a 5-kilometer highway featuring both an on-ramp (Section 7) and an off-ramp (Section 5). This highway was divided into 10 sections (S1-S10), each one measuring 500 m, corresponding to the sections used in the macroscopic model. Measurements of outflow and mean speed were collected every 10 seconds for each

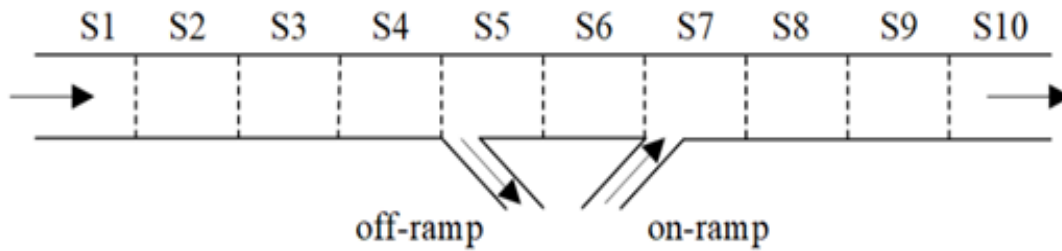


Figure 5.1: A schematic representation of the highway sections utilized for the simulations with the off-ramp located at S5 and the on-ramp located at S7.

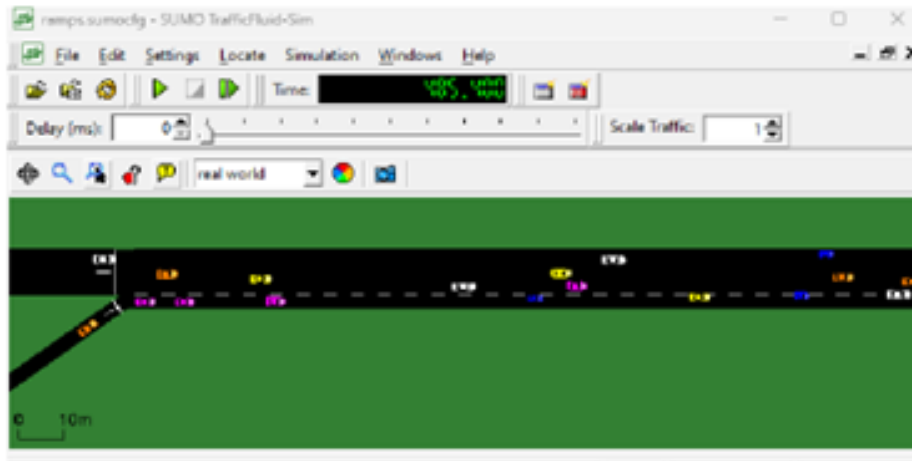


Figure 5.2: A snapshot of the TrafficFluid-Sim software.

section, providing data for comparison with the macroscopic model results in the objective function.

The dimensions of the vehicles adhered to a uniform distribution across six "dimension classes" is detailed in Table 5.1. Additionally, the desired longitudinal speed for each vehicle was randomly assigned within the range of 90 to 126 km/h, following a uniform distribution.

Separate simulations were carried out for various highway widths, starting with a nominal width of 10.2 m (equivalent to the width of three conventional lanes) and adjusted by increments or decrements of 0.85 meters (equivalent to one-quarter of a conventional lane). Consequently, the highway widths utilized in the simulations at both the microscopic and macroscopic levels were: 6.8m, 7.65m, 8.5m, 9.3m, 10.2m, 11.05m, 11.9m, and 12.75m. This range of widths was accompanied by varying levels of mainstream demand to ensure the activation of bottlenecks at the merging areas, leading to congestion that propagated back through several sections of the highway. This approach was necessary to obtain calibration data encompassing the entire spectrum of traffic conditions, including free flow, critical, and congested states.

In addition to varying widths and demand levels, the simulations also incorporated different force conditions. Specifically, simulations were conducted with no nudging forces applied ($\gamma_x = 0, \gamma_y = 0$), half nudging forces ($\gamma_x = 0.5, \gamma_y = 0.5$) and full nudging forces ($\gamma_x = 1, \gamma_y = 1$).

	Class 1	Class 2	Class 3	Class 4	Class 5	Class 6
Length (m)	3.20	3.90	4.25	4.55	4.60	5.15
Width (m)	1.60	1.70	1.80	1.82	1.77	1.84

Table 5.1: The different dimensions of vehicles used in the simulation experiment.

5.2 The Calibration Procedure in CALISTO

After obtaining the macroscopic data from the microscopic simulation, the next step involved implementing the calibration procedure using CALISTO.

Within the CALISTO software tool, the first step involves defining the network geometry. The highway geometry is precisely as depicted in Figure 5.1. Subsequently, the data from microscopic simulations are utilized as input, and the simulation step is defined, along with the weights for calculating the performance index. Following this, the model to be calibrated must be selected. Upon selection, the user must input initial values for both the global parameters and FD parameters of the model. These variables characterize the simulation frames, within which the functionality of the model can be observed and analyzed. The initial values of the variables, as discussed in Section 4.2, form the initial simplex, which is continuously refined through the Nelder-Mead optimization method.

For the original CTM model, the initial simplex is established by setting the values $\lambda_r = 1$ and $\lambda_d = 0$ for the global parameters, while initial values are also assigned to the FD parameters (v_f , w , and Q_{cap}) along with their respective boundaries. In the Extended Version of the CTM, the same approach is followed, with the distinction that the global parameters λ_r and λ_d take values within the range $[0,1]$.

In the first-order model with drivers' anticipation, two global parameters must be defined in detail: β and \tilde{v} , along with their respective maximum and minimum values. As previously mentioned, $0 < \beta \leq 1$ is a model parameter that adjusts the influence of anticipation, while \tilde{v} is a model parameter used in the function that determines the outflow from a highway section. In addition to these global parameters, there are also fundamental parameters— v_f , ρ_{cr} , Q_{cap} —each with their own maximum and minimum constraints that need to be specified.

The sole difference in the model parameters window of CALISTO for the extended version of drivers' anticipation model is the inclusion of the β_2 term. It is important to note that in this model, the sum of the variables β_1 and β_2 cannot exceed 0.5, as values beyond this threshold result in inaccurate model outputs. This constraint ensures that the model appropriately prioritizes the current section. Specifically, when examining the flow function from one section to another, the term q_i is multiplied by the factor $(1 -$

$\beta_1 - \beta_2$). This observation highlights the necessity of maintaining the sum of β_1 and β_2 within the specified limit to achieve reliable simulation results.

Once the calibration process for the model selected by the user is completed, the output will consist of the optimal values for both the global parameters and FD parameters. These optimal values are those that allow the model's calculations to align as closely as possible with the data from the microscopic simulations.

Chapter 6

Results

6.1 Simulations of Original CTM

The macroscopic simulations were conducted using the CALSITO software on a 5 km highway, identical to the one used for the microscopic simulations. This highway features an off-ramp at Section 5 and an on-ramp at Section 7, representing a typical highway environment with merging and diverging traffic flows.

As we have mentioned in Section 3.4, the CTM is a macroscopic traffic flow model that represents traffic dynamics on a road network using a discrete-time and discrete-space approach. The model is grounded in the kinematic wave theory of traffic flow, which is a form of the conservation law describing the movement of traffic.

The original CTM is known to be incapable of replicating the capacity drop phenomenon, which is the empirical observation that traffic flow at the onset of congestion is lower than the maximum flow of the highway. This capacity drop in conventional traffic is attributed to the limited and variable acceleration capabilities of different vehicles.

First, let us analyze the behavior of the original CTM under the conditions of an 8.5-meter-wide highway and no nudging. During peak demand, a bottleneck at the merging area in Section 7 (S7) is activated around $t = 24 \text{ min}$, causing congestion that propagates upstream, affecting several sections. The calibrated macroscopic model's space-time diagrams for speed and flow, shown in Figure 6.1 and Figure 6.2, indicate that the traffic conditions observed with microscopic lane-free automated vehicle traffic are accurately replicated by the macroscopic traffic flow model.

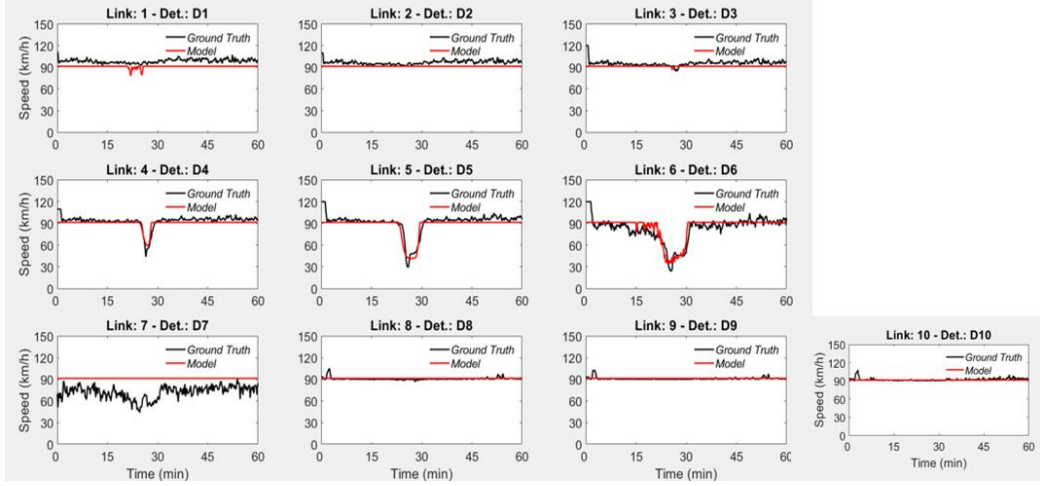


Figure 6.1: Space-time diagrams of microscopically produced speed (ground truth) versus macroscopic model estimates (model) for highway width of 8.5 m and no nudging for original CTM.

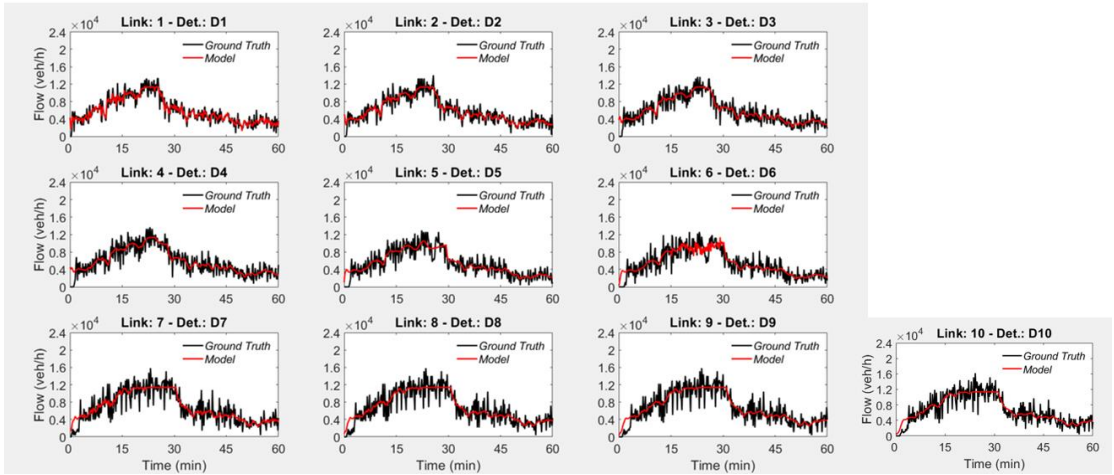


Figure 6.2: Space-time diagrams of microscopically produced flow (ground truth) versus macroscopic model estimates (model) for highway width of 8.5 m and no nudging for original CTM.

Figure 6.1 illustrates an interesting phenomenon: at $t = 24 \text{ min}$, an increased demand flow occurs in Section 7 (S7) causing congestion. This model predicts a reduction in speed within Sections 6 (S6), 5 (S5), and 4 (S4), which propagates upstream with satisfactory accuracy. However, at the bottleneck in S7, the model is unable to manage the congestion effectively, resulting in no reduction in speed; it remains close to free-flow speed. The traffic conditions in Sections 3 (S3), 2 (S2), and 1 (S1) normalize, with speeds maintaining close to free-flow speed.

In Figure 6.2, the model's inability to replicate the sudden decrease in capacity becomes evident. In Section 7 (S7), the ground truth data shows a decline in capacity following an initial rise. However, the model maintains a constant flow, depicted as a horizontal line, failing to capture this dynamic change accurately.

In a second simulation scenario, where the highway width is 10.2 meters and for the half nudging case, we observe again that the original CTM model cannot reproduce the capacity drop phenomenon. This is evident from the fact that, at Section 7, despite the reduction in flow in the real data (black line), the model (red line) maintains the flow at high values, following a horizontal trajectory

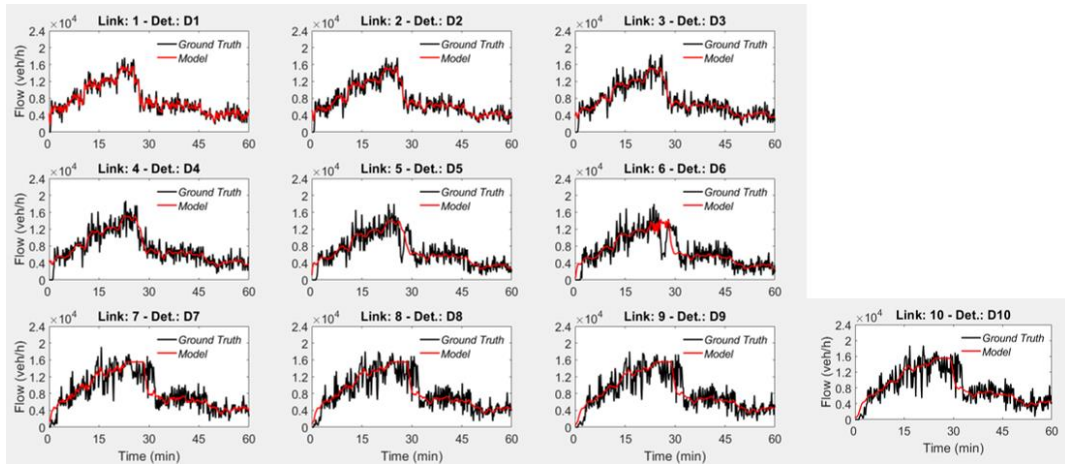


Figure 6.3: Space-time diagrams of microscopically produced flow (ground truth) versus macroscopic model estimates (model) for highway width of 10.2 m and half nudging for original CTM.

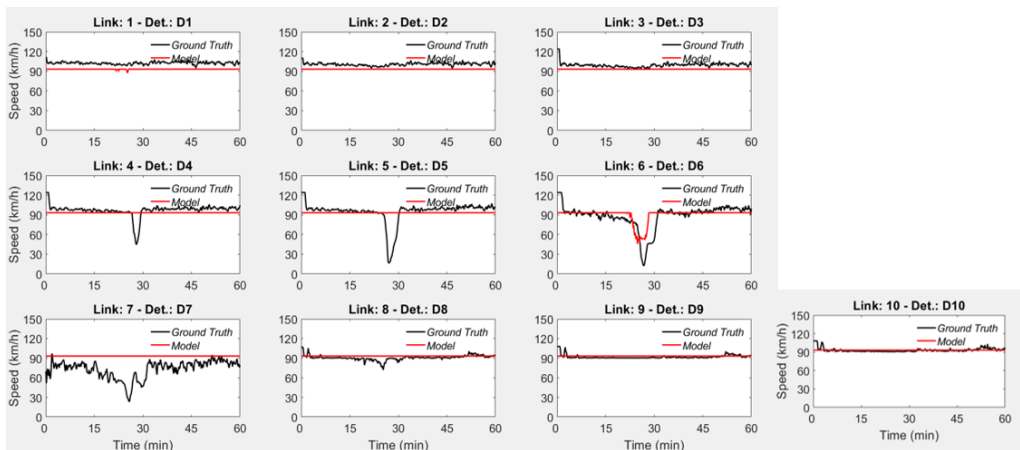


Figure 6.4: Space-time diagrams of microscopically produced speed (ground truth) versus macroscopic model estimates (model) for highway width of 10.2 m and half nudging for original CTM.

A series of macroscopic simulations were conducted for this model aiming to minimize the discrepancies from the microscopic simulations performed across eight various widths, including conditions of no nudging, half nudging, and full nudging. First, we analyze the trajectory of the objective function values for the original CTM.

Figure 6.5 displays the expected outcomes: the objective function values for the no nudging scenario are lower (i.e., better) than those for the half nudging scenario, which are subsequently lower than those for the full nudging scenario. This behavior indicates the difficulty of the model in accurately replicating the ground data at high nudging values.

Width (m)	No nudging	Half nudging	Full nudging
6.8	22.95	27.53	30.88
7.65	23.53	27.69	27.7
8.5	24.49	30.82	30.69
9.3	24.23	31.01	36.85
10.2	24.72	31.51	32.6
11.05	26.56	33.33	34.29
11.9	26.63	36.05	36.7
12.75	27.09	35.74	-

Table 6.1: The objective function values for each width and nudging scenario in the original CTM.

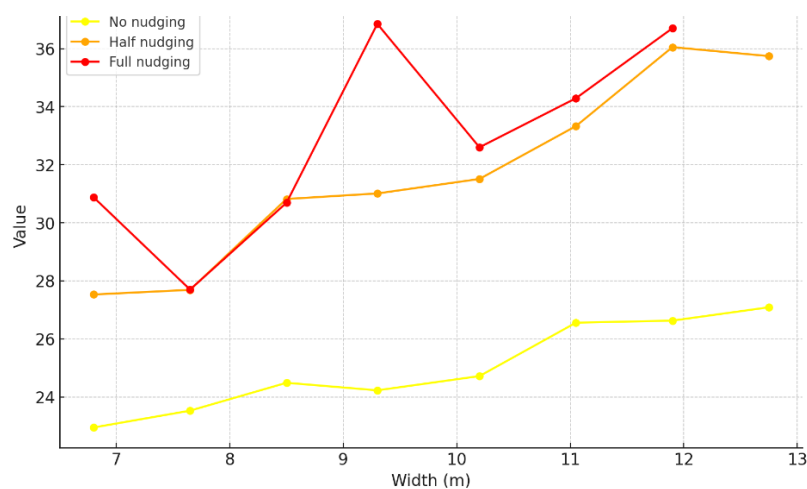


Figure 6.5: Line graph representing the model's objective function values based on the various highway widths and nudging scenarios (No nudging, Half nudging, and Full nudging) for original CTM.

We proceed to a detailed examination of the optimized variables. In this model we optimize the variables capacity flow (Q_{cap}), free flow speed (v_f) and wave speed (w). Then we calculated the ρ_{cr} values from the formula $\rho_{cr} = \frac{Q_{ap}}{v_f}$.

The calibrated critical density values obtained for various highway widths and different nudging strengths are illustrated in Figure 6.6. The results indicate that critical density increases with highway width. Additionally, it is evident that critical density also rises with increasing vehicle nudging strength for any given width. Quantitatively, the figure displays the lines generated via linear regression without the intercept term, implying that critical density is directly proportional to width for each nudging scenario. The calculated coefficients of determination r^2 , are 0.935, 0.934, and 0.926 for the full nudging, weak nudging, and no nudging cases, respectively.

Figure 6.7 demonstrates a linear correlation between highway width and calibrated capacity. The results indicate that capacity increases with highway width. Furthermore, an additional increase in capacity is observed with elevated levels of vehicle nudging, as depicted in Figure 6.7. The calculated coefficients of determination r^2 for capacity, are 0.931, 0.944, and 0.946 for the full nudging, weak nudging, and no nudging cases, respectively.

Regarding the free flow speed (Figure 6.8), it remains largely unaffected by variations in highway width. However, there is a slight increase in free flow speed corresponding with elevated levels of vehicle nudging.

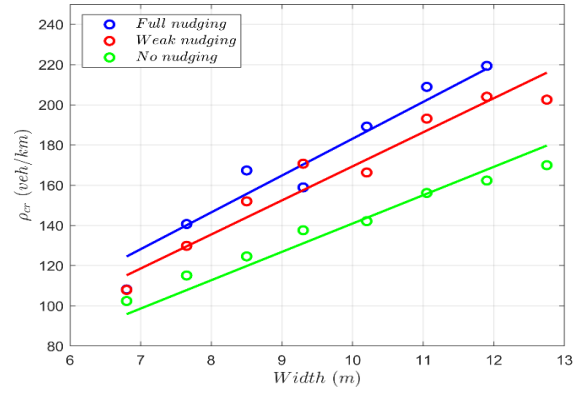


Figure 6.6: Critical density versus highway width for full, weak, and no nudging for original CTM.

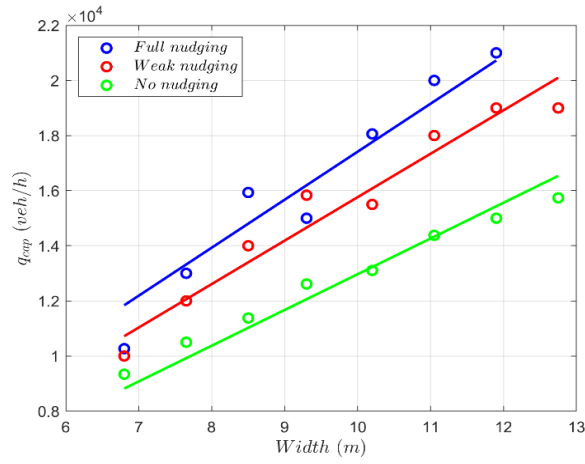


Figure 6.7: Capacity versus highway width for full, weak, and no nudging for original CTM.

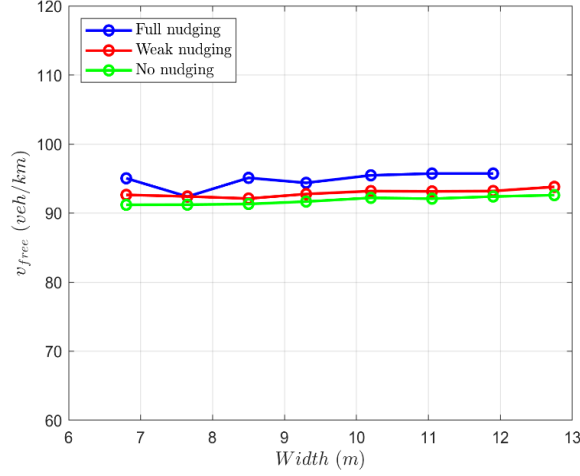


Figure 6.8: Free flow speed versus highway width for full, weak, and no nudging for original CTM.

6.2 Simulations of Extended Version of CTM

The extended version of CTM, as detailed in Section 3.4, introduces parameters λ_d (which determines the proportion of mainstream flow) and λ_r (which determines the proportion of on-ramp flow). This modification enables the model to be capable of replicating the capacity drop phenomenon.

We begin by analyzing the behavior of the extended CTM on a 10.2-meter-wide highway under half nudging conditions. At peak demand, a bottleneck forms in Section 7 (S7) around $t = 24 \text{ min}$, causing congestion that spreads upstream. The space-time diagrams for speed and flow in Figure 6.10 and Figure 6.9 show that the macroscopic model closely replicates the traffic conditions observed in the microscopic lane-free automated vehicle simulations.

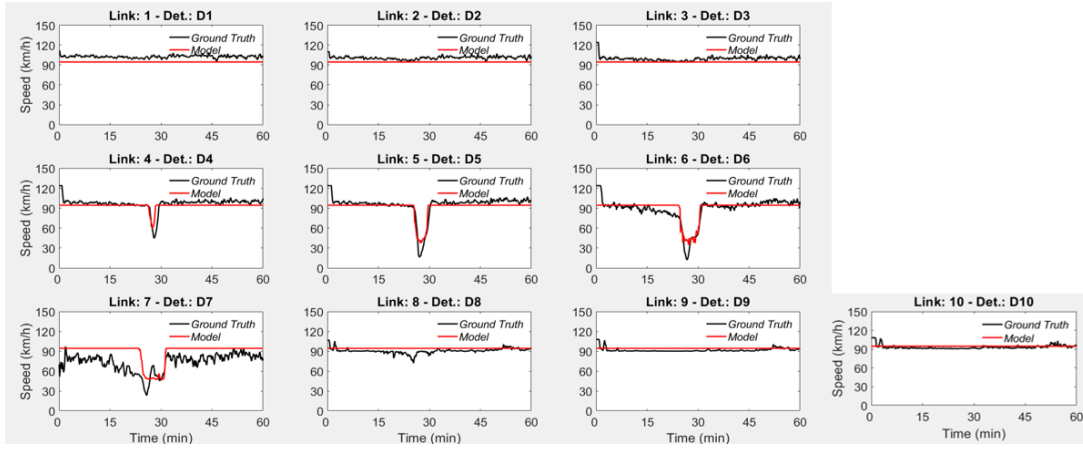


Figure 6.10: Space-time diagrams of microscopically produced speed (ground truth) versus macroscopic model estimates (model) for highway width of 10.2 m and half nudging for extended version of CTM.

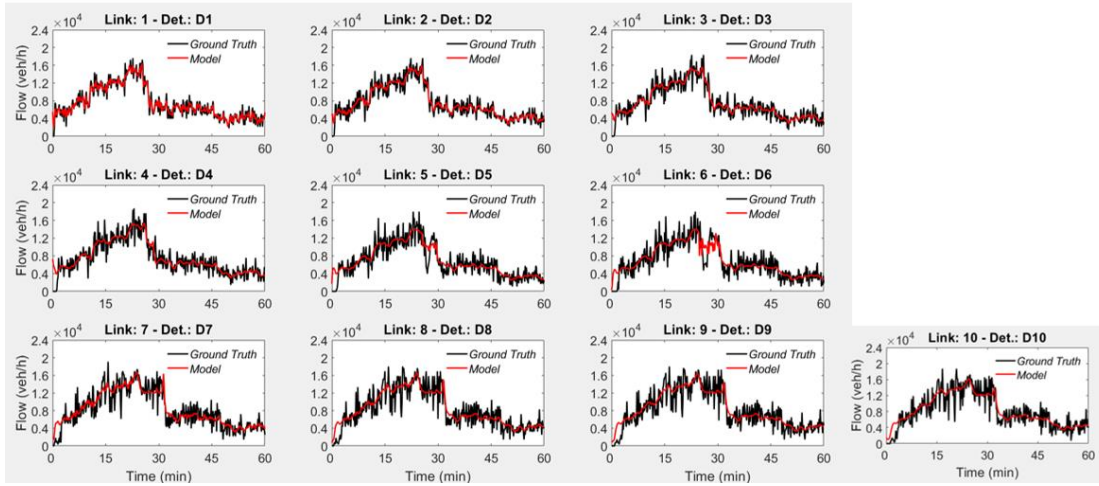


Figure 6.9: Space-time diagrams of microscopically produced flow (ground truth) versus macroscopic model estimates (model) for highway width of 10.2 m and half nudging for extended version of CTM.

In Figure 6.10, it is observed that the increased demand flow in Section 7 (S7) at $t = 24 \text{ min}$ causes a significant reduction in speed relative to the free flow speed. This reduction propagates upstream, affecting Sections 6 (S6), 5 (S5), and 4 (S4). The traffic conditions normalize in Sections 3 (S3), 2 (S2), and 1 (S1), where the speed is close to free-flow speed. It is also observed that the speeds predicted by the model under normal traffic flow conditions are stable and exhibit no fluctuations, a behavior that can be attributed to the mathematical formulation of the model, specifically as defined by Equation 3.19 and 3.20. In Figure 6.9, the model satisfactorily follows the flow.

In scenario 11.9 m highway width and full nudging at Section 7 (S7), the disturbances in the real data are much more pronounced compared to previous scenario. And yet, as we can see in Figure 6.12, the model accurately captures the initial flow drop (capacity drop) in terms of timing; however, it later flattens out.

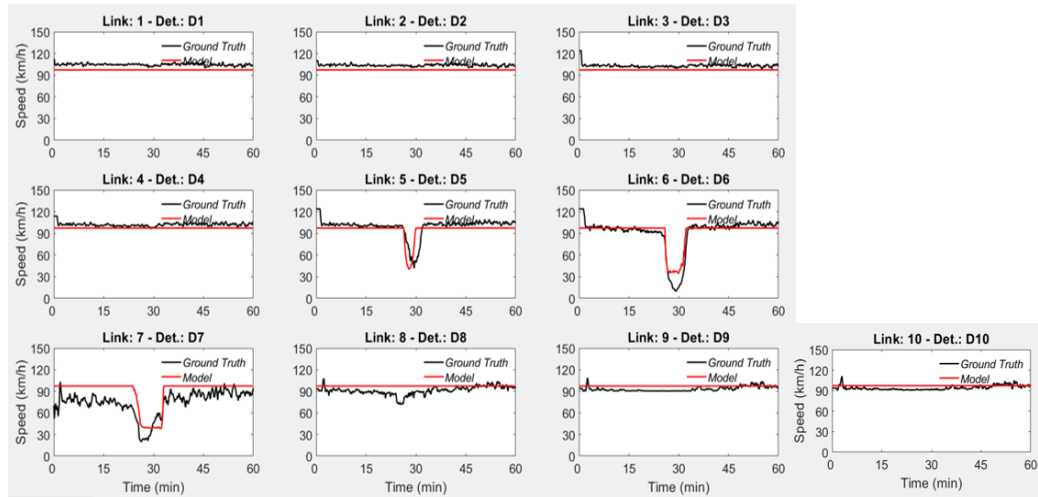


Figure 6.11: Space-time diagrams of microscopically produced speed (ground truth) versus macroscopic model estimates (model) for highway width of 11.9 m and full nudging for extended version of CTM.

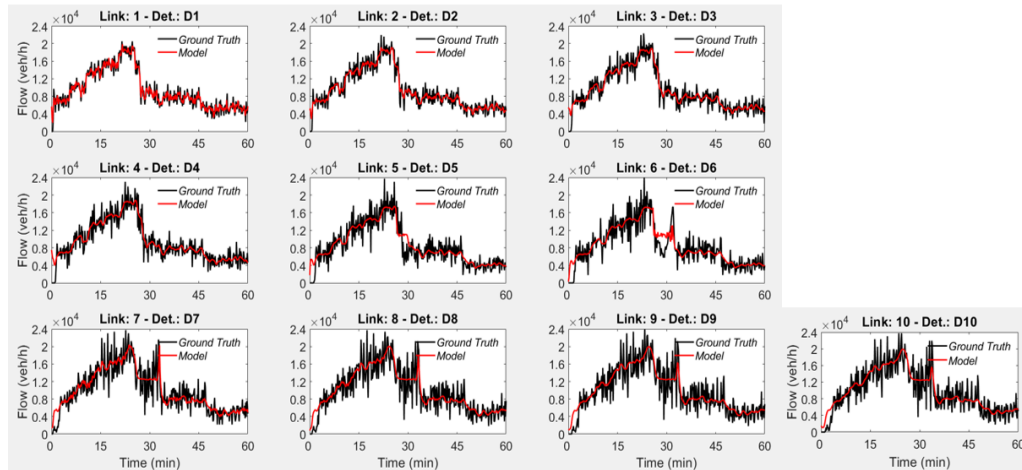


Figure 6.12: Space-time diagrams of microscopically produced flow (ground truth) versus macroscopic model estimates (model) for highway width of 11.9 m and full nudging for extended version of CTM.

To interpret the model results, we utilize the primary measure of comparison: the objective function value.

Width (m)	No nudging	Half nudging	Full nudging
6.8	21.87	24.87	26.02
7.65	22.81	24.88	27.69
8.5	23.86	26.71	26.85
9.3	23.53	26.07	28.45
10.2	24.43	26.59	27.86
11.05	25.72	28.25	28.63
11.9	25.34	28.77	29.93
12.75	26.17	27.82	-

Table 6.2: The objective function values for each width and nudging scenario in the extended version of CTM.

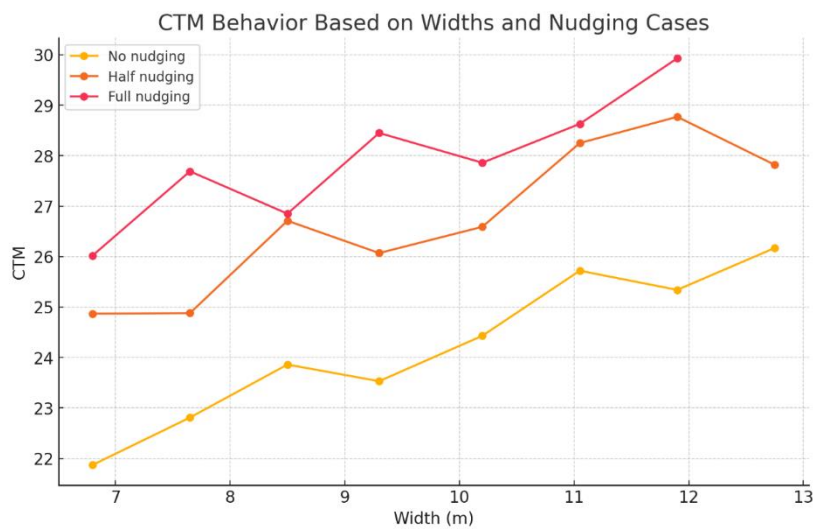


Figure 6.13: Line graph representing the model's objective function values based on the various highway widths and nudging scenarios (No nudging, Half nudging, and Full nudging) for extended version of CTM.

Figure 6.13 presents the anticipated results: the objective values for the no nudging scenario are lower (i.e., better) than those for the half nudging scenario, which are, in turn, lower than those for the full nudging scenario. This outcome is expected, as increasing the nudging force and the highway width between vehicles leads to greater system disturbance, indicating that the model deviates more from the ground truth data.

The subsequent figures illustrate the anticipated outcomes concerning the model's optimization variables: critical density, capacity flow, and free-flow speed. Notably, the critical density demonstrates a linear increase with the expansion of highway widths. Additionally, across all widths, the full nudging scenario consistently exhibits higher values compared to the half nudging and no nudging scenarios. The calculated coefficients of determination r^2 for critical density are 0.835, 0.885, and 0.833 for the full nudging, weak nudging, and no nudging scenarios, respectively. A similar trend is observed for capacity flow, with r^2 values of 0.928, 0.921, and 0.782 for the full nudging, weak nudging, and no nudging scenarios, respectively. In contrast, the free-flow speed remains largely insensitive to highway width but shows slight sensitivity to the different nudging scenarios.

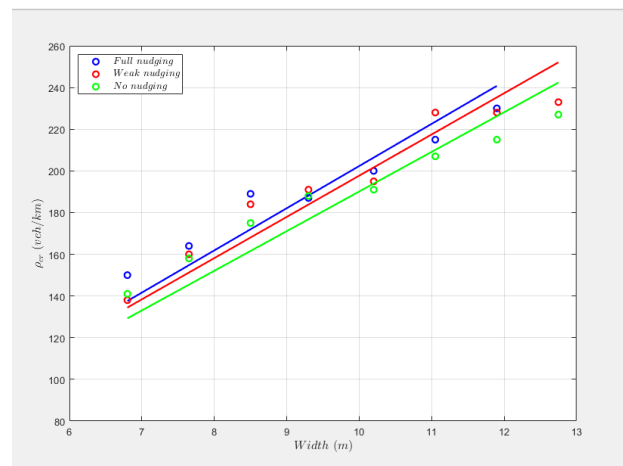


Figure 6.14: Critical density versus highway width for full, weak, and no nudging for extended version of CTM.

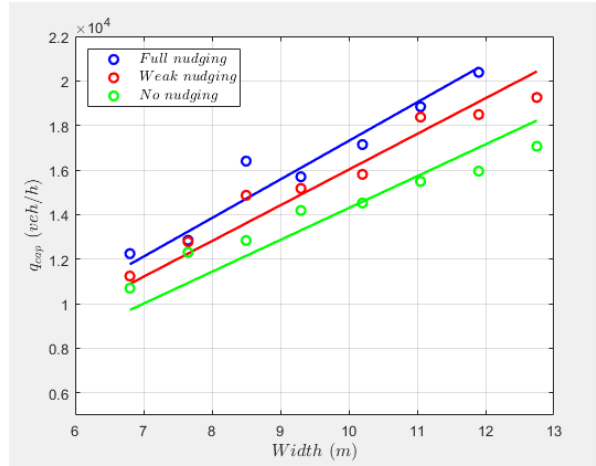


Figure 6.16: Capacity versus highway width for full, weak, and no nudging for extended version of CTM.

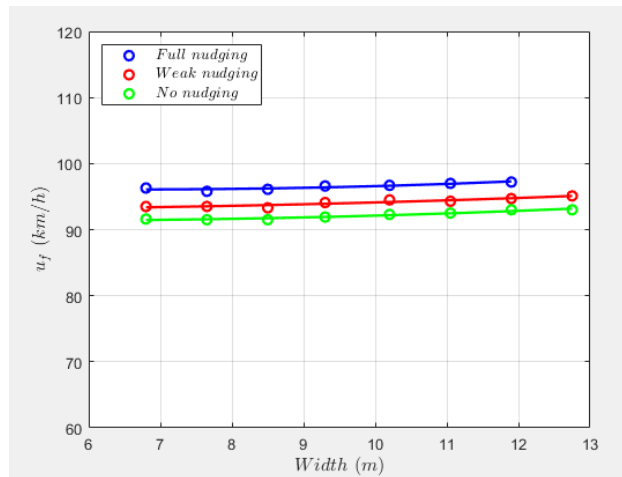


Figure 6.15: Free flow speed versus highway width for full, weak, and no nudging for extended version of CTM.

6.3 Simulations of First Order Model with Driver's Anticipation

This model, along with its extension, forms the foundation of this thesis. Let us now examine the results obtained from the simulations. For the scenario with an 8.5-meter highway width and no vehicle nudging, the following speed and flow plots are derived.

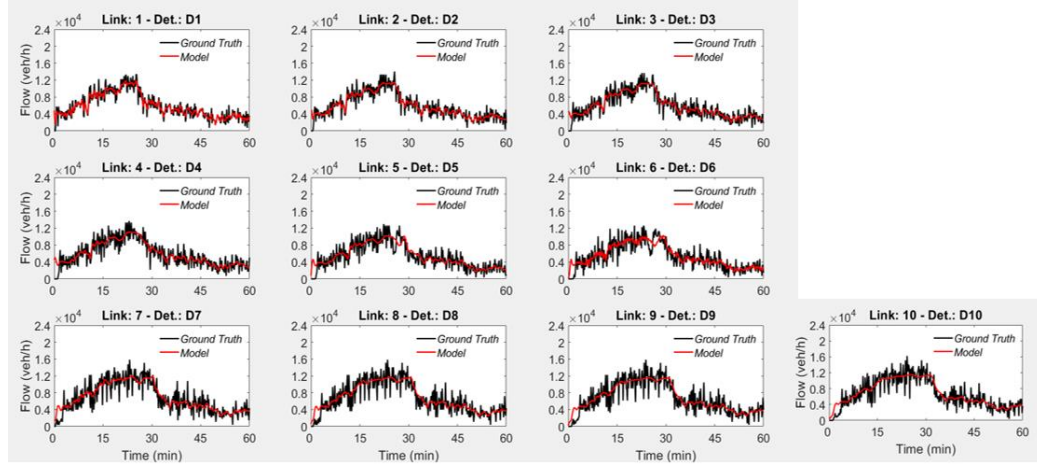


Figure 6.17: Space-time diagrams of microscopically produced flow (ground truth) versus macroscopic model estimates (model) for highway width of 8.5 m and no nudging for driver's anticipation model.

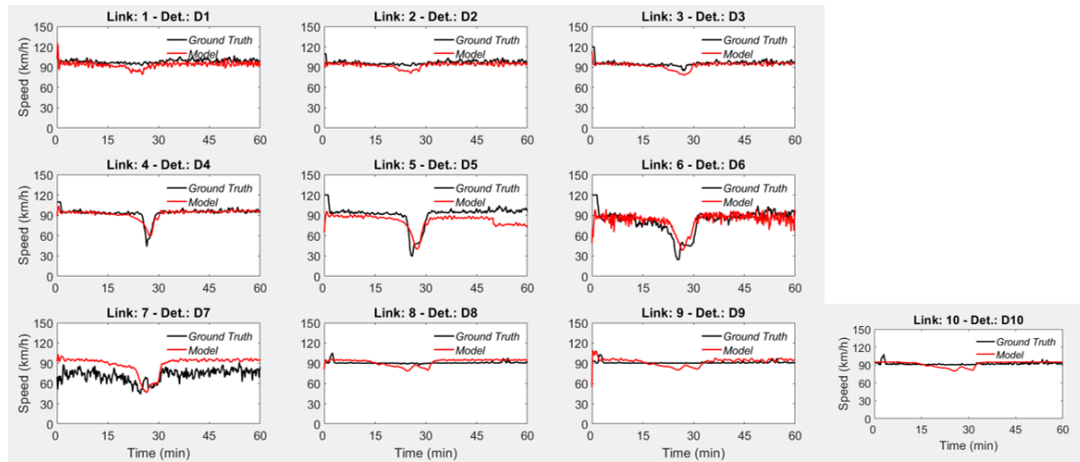


Figure 6.18: Space-time diagrams of microscopically produced speed (ground truth) versus macroscopic model estimates (model) for highway width of 8.5 m and no nudging for driver's anticipation model.

Due to the mathematical characteristics of the model, Figure 6.18 reveals that the calculated speed fluctuates based on variations in the ground truth, unlike in CTM where speeds remain more stable, exhibiting horizontal movement during free flow conditions. As previously discussed, during period of peak demand, a bottleneck is activated at the merging area in Section 7 (S7), resulting in congestion that propagates upstream and impacts multiple sections. Specifically, at S7, the merge area causes a reduction in speed, which then propagates upstream, affecting Sections 6 (S6), 5 (S5), and 4 (S4). Traffic conditions normalize in Sections 3 (S3), 2 (S2), and 1 (S1), where the speed maintains the free flow level. With reference to the flow plot (Figure 6.17), the model identifies a slight decrease at the onset of the drop capacity phenomenon in S7.

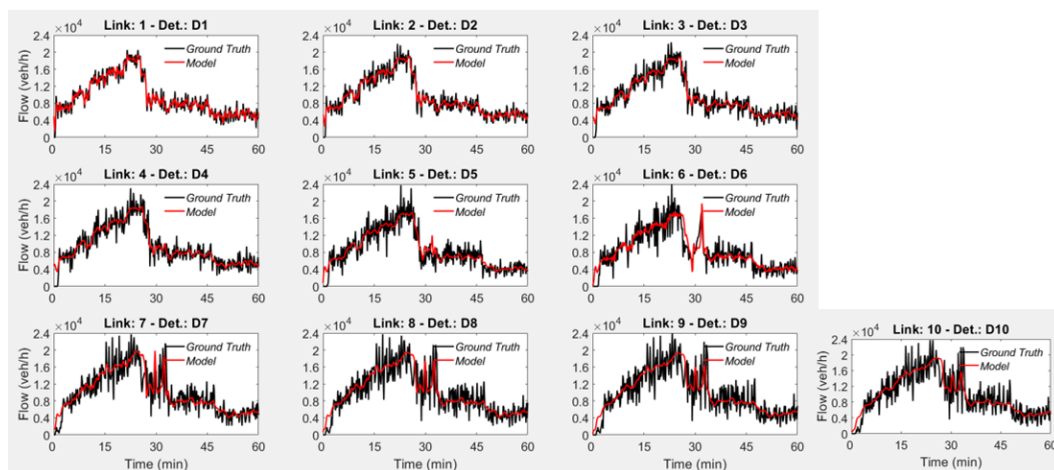


Figure 6.19: Space-time diagrams of microscopically produced flow (ground truth) versus macroscopic model estimates (model) for highway width of 11.9 m and full nudging for driver's anticipation model.

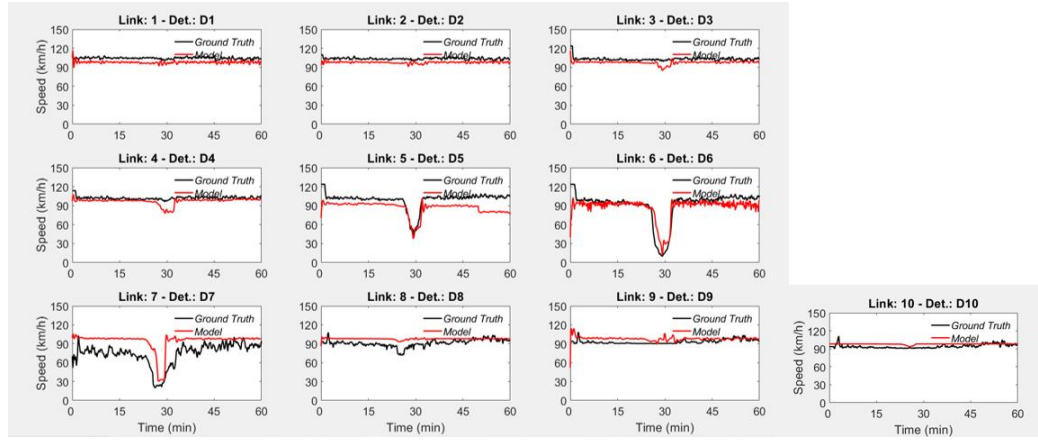


Figure 6.20: Space-time diagrams of microscopically produced speed (ground truth) versus macroscopic model estimates (model) for highway width of 11.9 m and full nudging for driver's anticipation model.

In this scenario (11.9 m highway width and full nudging), where the ground truth at Section 7 (S7) shows a significant speed drop at $t = 24 \text{ min}$ (Figure 6.20), the model can predict also the capacity drop at S7, albeit with a slight time delay (Figure 6.19).

In relation to the objective function values, it is observed in this model that the values for the no nudging scenario are lower (i.e., better) than those for the half nudging scenario, which, in turn, are lower than those for the full nudging scenario.

Width (m)	No nudging	Half nudging	Full nudging
6.8	23.5	25.21	27.72
7.65	23.86	26.64	28.52
8.5	25.28	29.12	28.69
9.3	24.53	27.8	28.69
10.2	25.65	29.82	31.67
11.05	26.82	31.73	31.73
11.9	26.49	32.64	33.04
12.75	27.66	31.41	

Table 6.3: The objective function values for each width and nudging scenario in the driver's anticipation model.

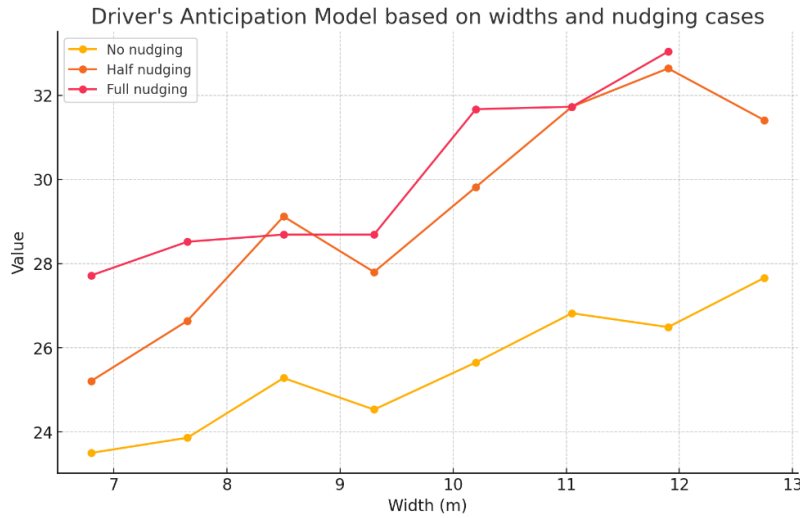


Figure 6.21: Line graph representing the model's objective function values based on the various highway widths and nudging scenarios (No nudging, Half nudging, and Full nudging) for driver's anticipation model.

The figures that follow illustrate the expected results in relation to the model's optimization variables, namely critical density (ρ_{cr}), capacity flow (Q_{cap}), and free flow speed (v_f). Specifically, the critical density exhibits a linear increase with the expansion of highway widths. Additionally, across all widths, the full nudging scenario consistently displays higher values compared to the half nudging and no nudging scenarios. The calculated coefficients of determination r^2 for ρ_{cr} , are 0.897, 0.906, and 0.931 for the full nudging, weak nudging, and no nudging cases, respectively. A similar pattern is observed for the capacity flow. The calculated coefficients of determination r^2 for Q_{cap} , are 0.974, 0.969, and 0.918 for the full nudging, weak nudging, and no nudging cases, respectively. In contrast, the free-flow speed remains largely insensitive to highway width but shows a slight sensitivity to the different nudging scenarios.

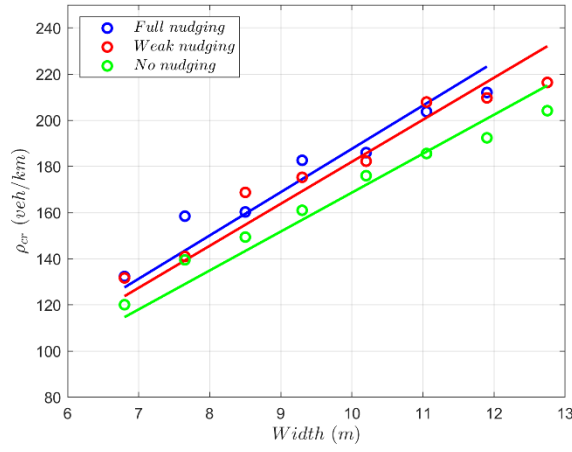


Figure 6.22: Critical density versus highway width for full, weak, and no nudging for driver's anticipation model.

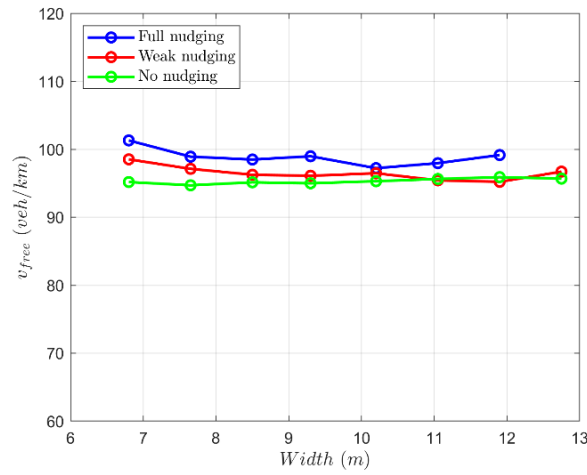


Figure 6.23: Free flow speed versus highway width for full, weak, and no nudging for driver's anticipation model.

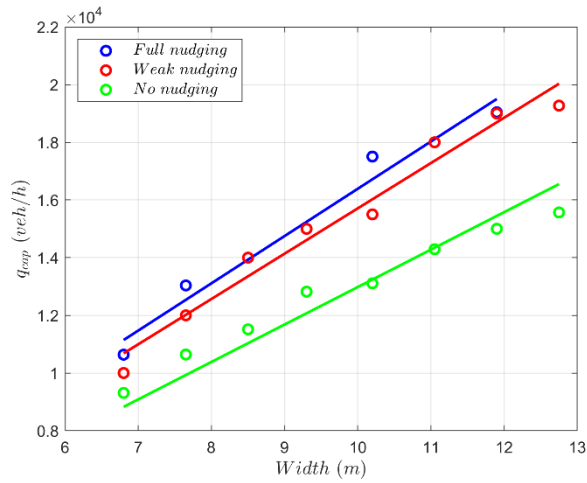


Figure 6.24: Capacity versus highway width for full, weak, and no nudging for driver's anticipation model.

In this model, the values of global parameters (β and \tilde{v}) are of particular interest, as they significantly influence the model's behavior. Across the simulation scenarios, the average β (Figure 6.25) was observed to be 0.62, 0.65, and 0.66 for no nudging, half nudging, and full nudging, respectively. Similarly, the values of \tilde{v} (Figure 6.26) exhibited some stability but showed no apparent pattern.

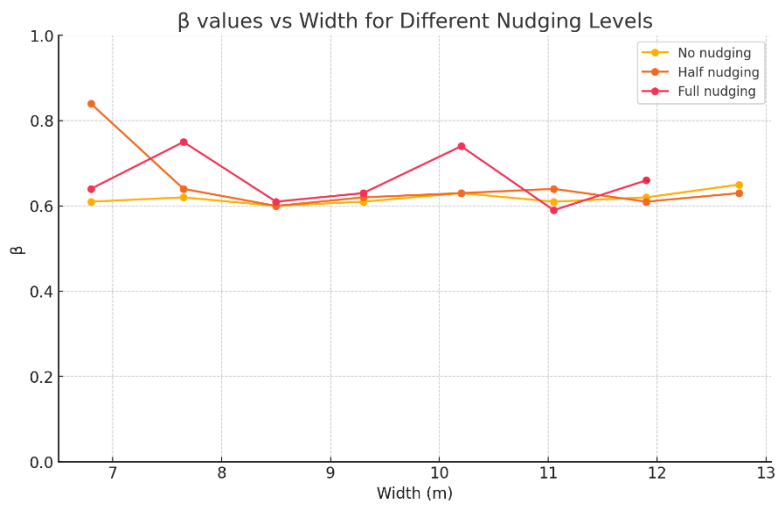


Figure 6.25: Line graph representing the model's global parameter β based on the various highway widths and nudging scenarios (No nudging, Half nudging, and Full nudging).

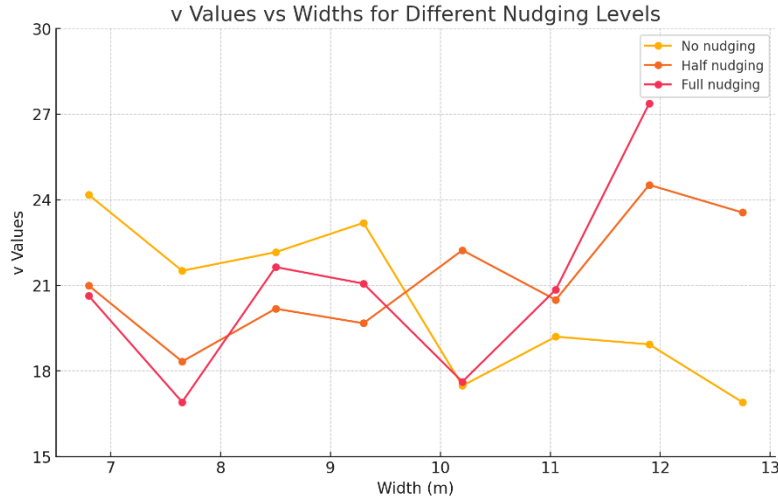


Figure 6.26: Line graph representing the model's global parameter \tilde{v} based on the various highway widths and nudging scenarios (No nudging, Half nudging, and Full nudging).

6.4 Simulations of Extended Version of the Drivers' Anticipation Model

As outlined in Section 3.6, the equation controlling the flow between sections in the current model incorporates a novel global parameter, β_2 . Including this variable adds useful information to the model, making it easier for the optimizer to find the best solutions. To illustrate the model's application, we now examine the scenario of a 9.3-meter-wide highway with half nudging, as simulated in CALISTO, through the lens of its speed and flow plots.

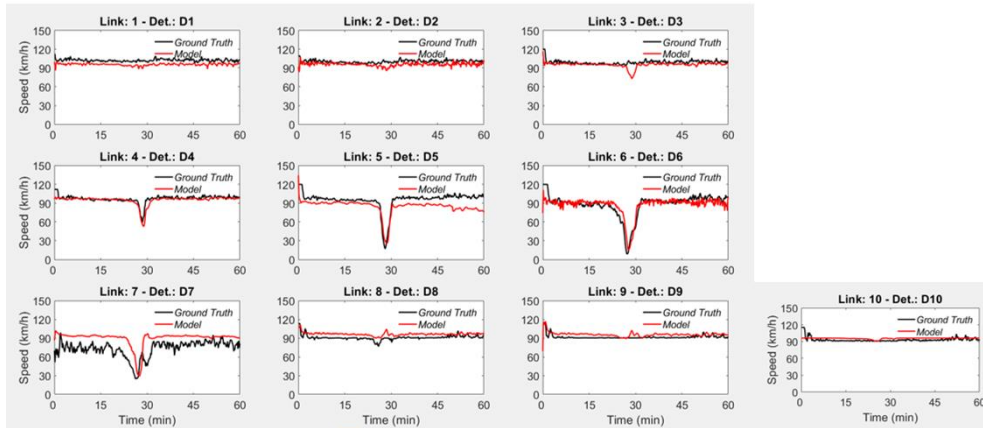


Figure 6.27: Space-time diagrams of microscopically produced speed (ground truth) versus macroscopic model estimates (model) for highway width of 9.3 m and half nudging for the extended version of driver's anticipation model.

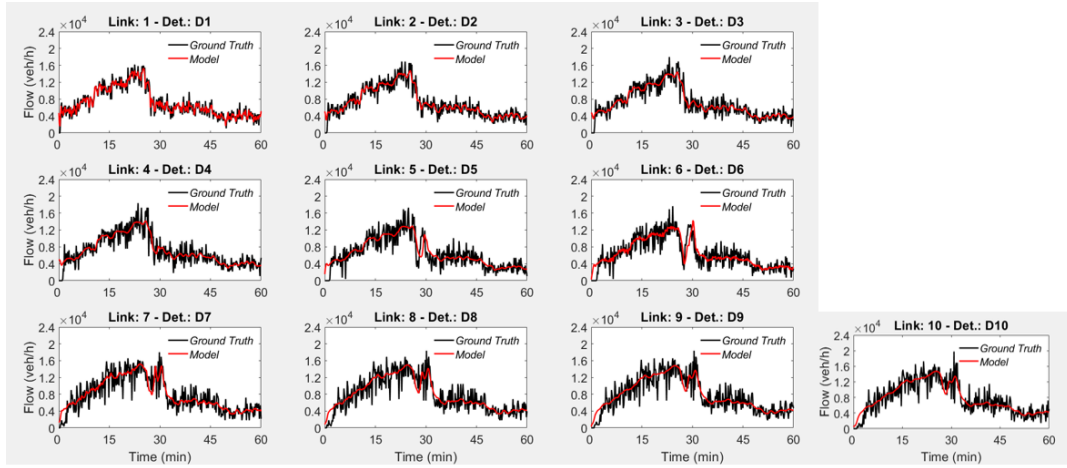


Figure 6.28: Space-time diagrams of microscopically produced flow (ground truth) versus macroscopic model estimates (model) for highway width of 9.3 m and half nudging for the extended version of driver's anticipation model.

In this scenario, the model not only captures the capacity drop at Section 7 (Figure 6.28) with precise timing ($t = 24 \text{ min}$) but also predicts some of the fluctuations until the overall flow decreases ($t > 30 \text{ min}$).

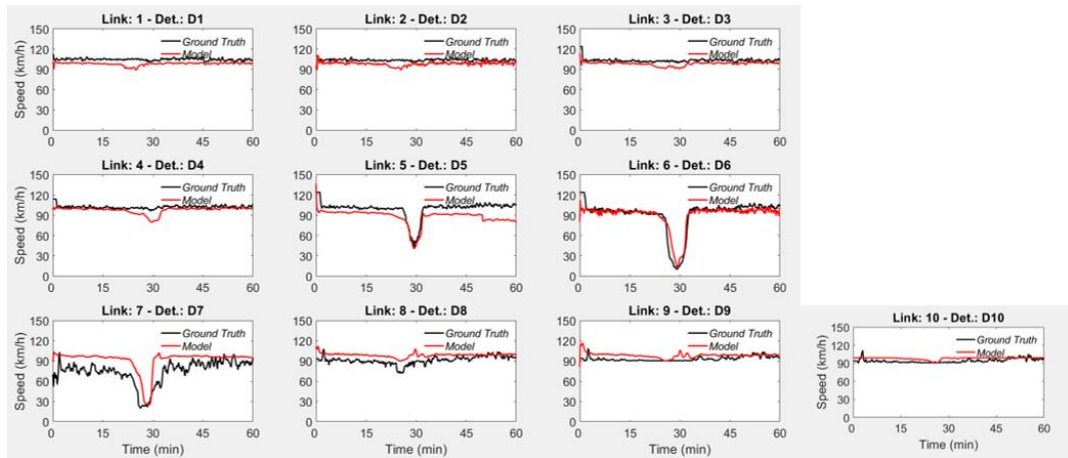


Figure 6.29: Space-time diagrams of microscopically produced speed (ground truth) versus macroscopic model estimates (model) for highway width of 11.9 m and full nudging for the extended version of driver's anticipation model.

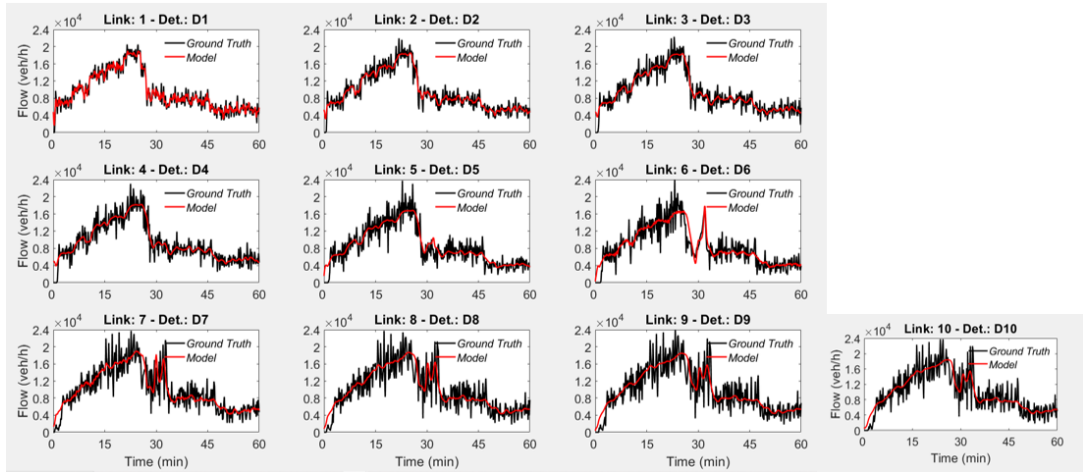


Figure 6.30: Space-time diagrams of microscopically produced flow (ground truth) versus macroscopic model estimates (model) for highway width of 11.9 m and full nudging for the extended version of driver's anticipation model.

In the 11.9 m highway width and full nudging scenario, the model demonstrates satisfactory performance within the merge area (S7), where the mainstream and on-ramp flows converge. Notably, the speed reduction propagates upstream, affecting multiple sections before gradually stabilizing near free-flow speeds in the first three sections. An analysis of the flow plot shows that the model provides a more accurate representation of flow fluctuations compared to the original driver anticipation model, effectively capturing abrupt variations in flow dynamics.

We will next examine how the overall performance, represented by the objective function value, changes across different highway widths and levels of vehicle nudging in our simulations.

Width (m)	No nudging	Half nudging	Full nudging
6.8	22.19	24.58	27.19
7.65	22.78	24.5	27.36
8.5	24.49	27.11	26.97
9.3	24.32	27.17	31.74
10.2	24.7	28.45	29.4
11.05	26.22	30.44	30
11.9	26.01	31.79	31.25
12.75	26.99	30.38	

Table 6.4: The objective function values for each width and nudging scenario in the extended version of driver's anticipation model.

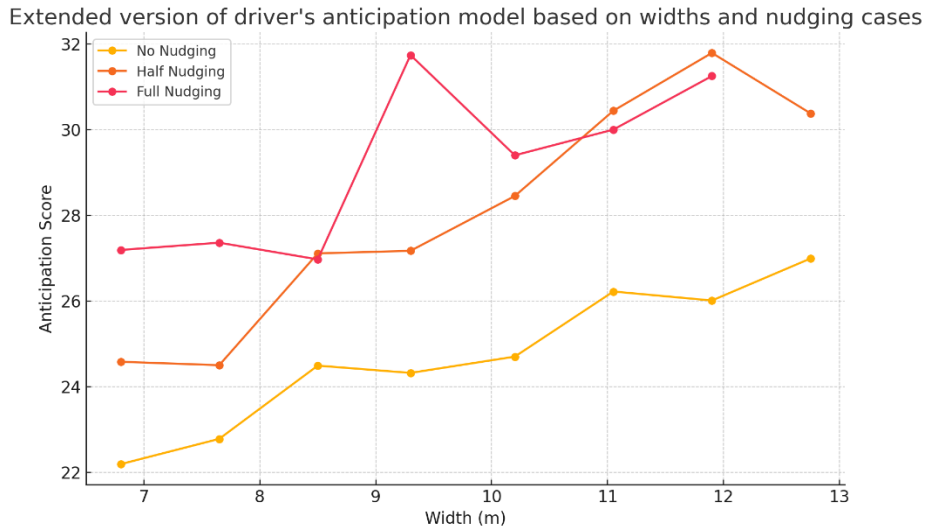


Figure 6.31: Line graph representing the model's objective function values based on the various highway widths and nudging scenarios (No nudging, Half nudging, and Full nudging) for the extended version of driver's anticipation model.

The no nudging scenario yields the lowest values, indicative of superior performance. This is followed by the half nudging scenario with intermediate values, while the full nudging scenario exhibits the highest objective values. Moreover, further improvement is observed in the objective function values when comparing the extended model to the original drivers' anticipation model across all nudging cases.

The subsequent figures present the model-derived relationships among highway width, nudging intensity, and key traffic parameters: critical density, capacity flow, and free flow speed. Critical density and capacity flow exhibit a strong positive correlation with highway width, with full nudging consistently yielding higher values than half nudging or no nudging. While free flow speed remains relatively unaffected by highway width, it is modestly influenced by nudging conditions. These findings are quantitatively supported by the coefficients of determination. More specifically, the calculated coefficients of determination r^2 for ρ_{cr} , are 0.719, 0.708, and 0.787 for the full nudging, weak nudging, and no nudging cases, respectively. Accordingly, for the Q_{cap} the coefficients are, 0.974, 0.962, and 0.872 for the full nudging, weak nudging, and no nudging cases, respectively.

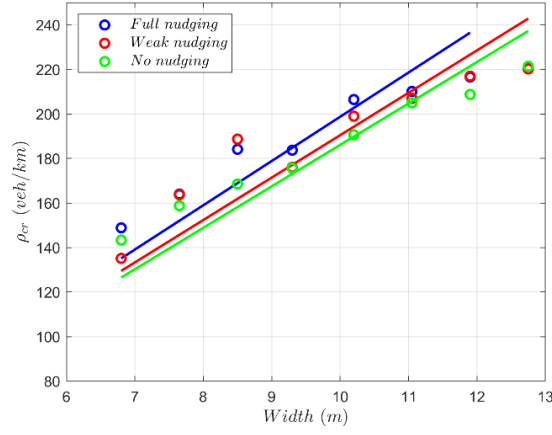


Figure 6.32: Critical density versus highway width for full, weak, and no nudging for the extended version of driver's anticipation model.

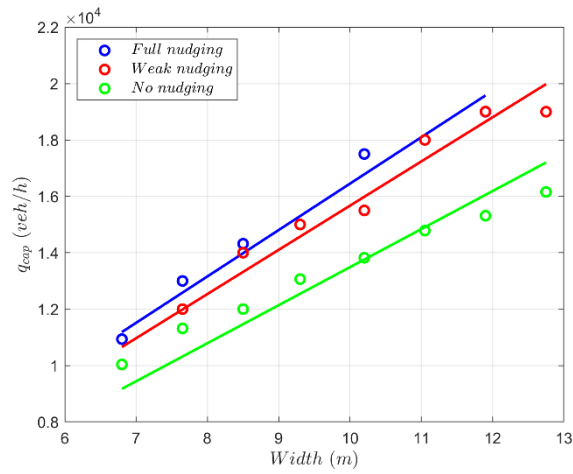


Figure 6.33: Capacity versus highway width for full, weak, and no nudging for the extended version of driver's anticipation model.

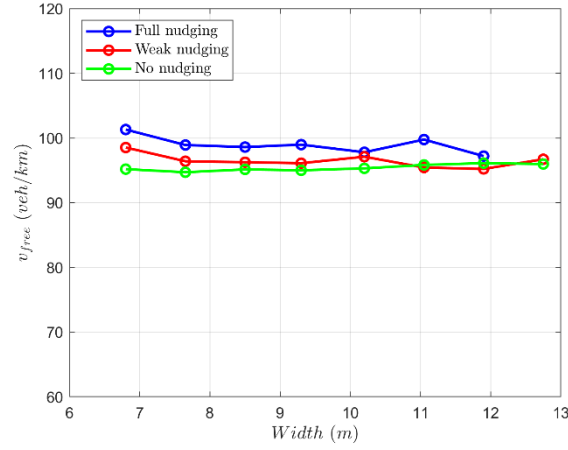


Figure 6.34: Free flow speed versus highway width for full, weak, and no nudging for the extended version of driver's anticipation model.

A critical aspect of this model is the behavior of the global parameters ($\beta_1, \beta_2, \tilde{v}$), as their values directly influence the model's accuracy. Analysis across simulation scenarios reveals that both β_1 and β_2 exhibit consistent values within a range [0.17, 0.23] demonstrating a degree of stability. It is important to reiterate that their sum must remain below 0.5. The values of \tilde{v} now span a wider range, from [9.5, 27].



Figure 6.35: Line graph representing the model's global parameter β_1 and β_2 based on the various highway widths and nudging scenarios (No nudging, Half nudging, and Full nudging).

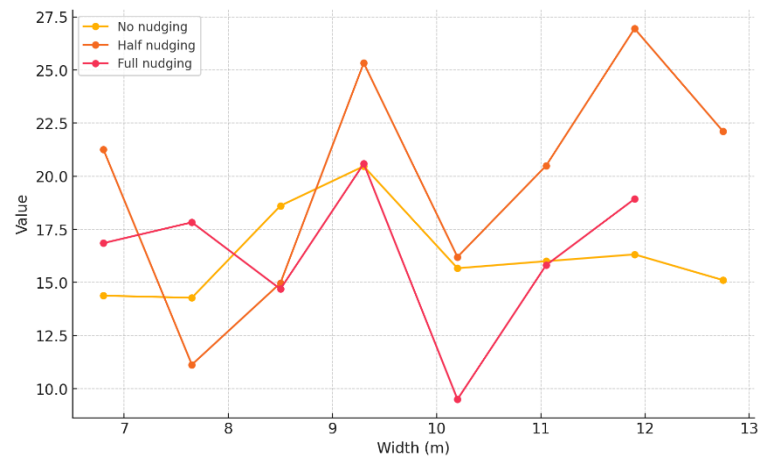


Figure 6.36: Line graph representing the model's global parameter \tilde{v} based on the various highway widths and nudging scenarios (No nudging, Half nudging, and Full nudging).

6.5 The Overall Comparison of Models

Considering the objective function value as the primary metric for comparing the models, the following graphs illustrate the progression of the objective function for each model across different nudging scenarios as the highway width incrementally increases.

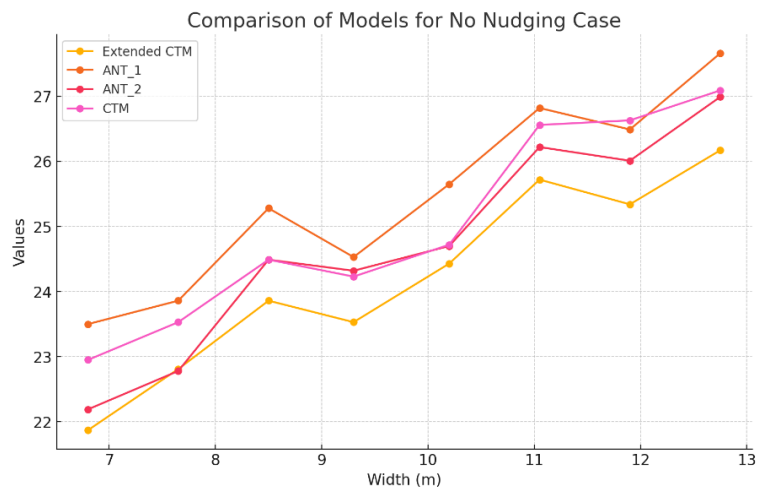


Figure 6.37: Line graph representing the objective function values of the 4 models based on the various highway widths and no nudging scenario.

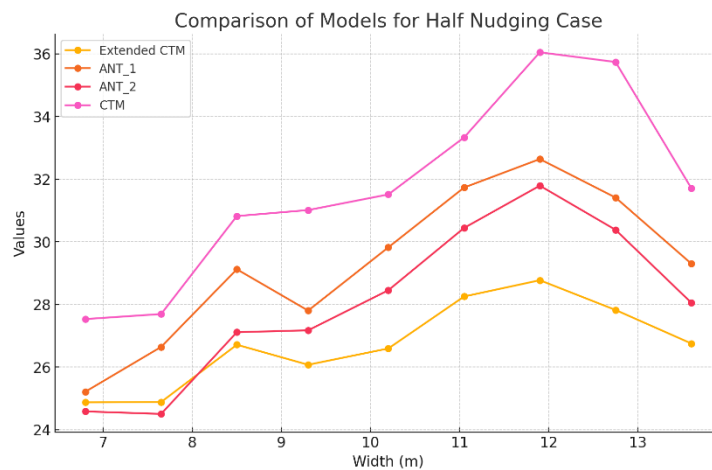


Figure 6.38: Line graph representing the objective function values of the 4 models based on the various highway widths and half nudging scenario.

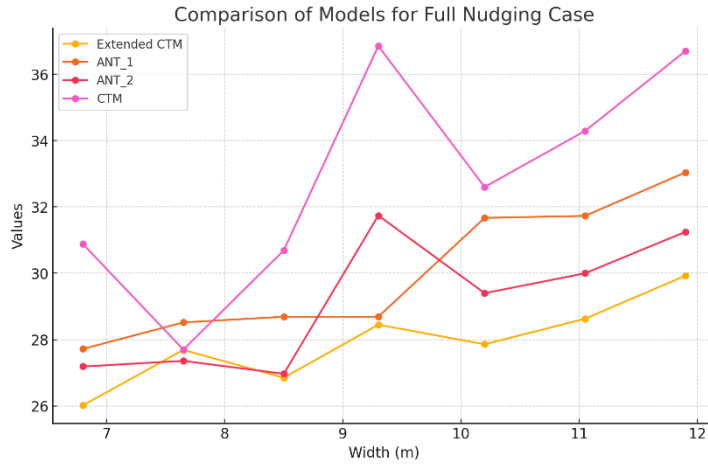


Figure 6.39: Line graph representing the objective function values of the 4 models based on the various highway widths and full nudging scenario.

The extended version of CTM, which simulates the effect of capacity drop, consistently achieves the best results across all three nudging scenarios, maintaining the lowest objective values. In contrast, the original CTM, except in the no nudging scenario where it reliably reduces speed in the upstream sections of the merge area and thereby decreases deviation from the ground truth, produces significantly higher objective values. This highlights the critical role of the capacity drop phenomenon in traffic flow modeling. Furthermore, the extended version of the drivers' anticipation model performs better than the original drivers' anticipation model, occasionally achieving lower objective values than the extended CTM. This behavior is expected, as the extended model has more degrees of freedom than the original. Notably, in both the half and full nudging scenarios, the original drivers' anticipation model outperforms the original CTM.

Chapter 7

Conclusion

This thesis has critically evaluated four first-order macroscopic models—the CTM, the Extended Version of CTM, the Drivers' Anticipation Model, and an Extended Version of the Drivers' Anticipation Model—applied to a simplified ten-section highway stretch featuring an off-ramp and an on-ramp. The performance of these models was assessed using data from microscopic simulations conducted within the TrafficFluid-Sim environment. The models were calibrated for this specific highway using the innovative CALISTO tool, which was expanded to accommodate the complexities of the Drivers' Anticipation Model and its extended variant.

The findings of this investigation reveal that the Extended Version of the Drivers' Anticipation Model is particularly effective in replicating real-world traffic conditions, outperforming the original Drivers' Anticipation Model and the original CTM in most scenarios. The extended model's ability to incorporate additional degrees of freedom allowed it to consistently achieve lower objective values, particularly in the half and full nudging scenarios, sometimes even surpassing the performance of the extended CTM. This indicates the importance of incorporating more sophisticated driver behavior dynamics, such as anticipation, into macroscopic models for more accurate traffic flow predictions.

Moreover, the original Drivers' Anticipation Model also showed considerable effectiveness, especially in the half and full nudging scenarios, where it outperformed the original CTM. This further underscores the value of including anticipation mechanisms in traffic modeling, as they contribute to a more realistic representation of driver behavior and traffic dynamics.

Regarding the extended version of CTM, according to the criterion of objective function values, this specific model demonstrates the best performance, as it consistently maintains the lowest objective function values in every scenario when compared to the other three models. The extended version of CTM is consistent in reducing speed at the onset of congestion at the bottleneck, as well as managing the spillback of speed reduction across some upstream sections. Additionally, a key factor

contributing to the superior performance of the model is its ability to predict the capacity drop phenomenon.

The original CTM demonstrates the worst performance, as its model calculations exhibit the greatest deviation from the ground truth when compared to the other three models. This is due to the model's inability to predict the capacity drop phenomenon. As a result, at the bottleneck where congestion occurs, the model fails to reduce speed, leading to a stable flow rather than a decrease. This clearly illustrates the importance of a macroscopic model's ability to incorporate capacity drop and effectively simulate congestion.

Regarding the variables optimized across all models, we observe consistent behavior. The variables highway capacity and critical density have shown a linear increase as highway width expands, with further increases observed when vehicle nudging is elevated. However, free flow speed remains unaffected by highway width, exhibiting only a slight increase with vehicle nudging. The Fundamental Diagrams (FD) of the CTM and its extended version are linear and, more specifically, triangular in shape, while the FD of the Drivers' Anticipation model and the extended version of Drivers' Anticipation are nonlinear.

In conclusion, this thesis demonstrates that macroscopic models can accurately replicate real-world traffic conditions while providing a broader perspective on highway properties. It is time to move beyond traditional traffic management and look forward to the future of traffic flow with Traffic Fluid.

BIBLIOGRAPHY

- [1] G. Dimitrakopoulos and P. Demestichas, "Intelligent Transportation Systems," in *IEEE Vehicular Technology Magazine*, vol. 5, no. 1, pp. 77-84, March 2010, doi: 10.1109/MVT.2009.935537.
- [2] Papageorgiou, M., Mountakis, K. S., Karafyllis, I., & Papamichail, I. (2019). Lane-free artificial-fluid concept for vehicular traffic. arXiv preprint arXiv:1905.11642.
- [3] C. Diakaki, M. Papageorgiou, I. Papamichail, and I. Nikolos, "Overview and analysis of vehicle automation and communication systems from a motorway traffic management perspective", *Transportation Research Part A*, 75, 2015, pp. 147–165.
- [4] E. Marti, M. A. De Miguel, F. Garcia, and J. Perez, "A review of sensor technologies for perception in automated driving," *IEEE Intelligent Transportation Systems Magazine*, vol. 11, no. 4, pp. 94–108, 2019.
- [5] Papageorgiou, M., Mountakis, K. S., Karafyllis, I., & Papamichail, I. (2019). Lane-free artificial-fluid concept for vehicular traffic. arXiv preprint arXiv:1905.11642.
- [6] <https://www.trafficfluid.tuc.gr/en/home>.
- [7] Papamichail, I., Schoenn-Anchling, N., Malekzadeh, M., Markantonakis, V., & Papageorgiou, M. (2023, September). Macroscopic Traffic Flow Model Calibration for Lane-free Automated Vehicle Traffic. In *2023 IEEE 26th International Conference on Intelligent Transportation Systems (ITSC)* (pp. 3485-3492). IEEE.
- [8] Daganzo, C. F. (1995). The cell transmission model, part II: network traffic. *Transportation Research Part B: Methodological*, 29(2), 79-93.
- [9] Kontorinaki, M., Spiliopoulou, A., Roncoli, C., & Papageorgiou, M. (2017). First-order traffic flow models incorporating capacity drop: Overview and real-data validation. *Transportation Research Part B: Methodological*, 106, 52-75.
- [10] Spiliopoulou, A., Markantonakis, V., Papamichail, I. and Papageorgiou, M. (2014-2024). "CALISTO (CALibrationS Tool) Manual". Chania, Crete, Greece.
- [11] Toledo, T., Koutsopoulos, H., Ben-Akiva, M., Jha, M. (2005). Microscopic Traffic Simulation: Models and Application. In: Kitamura, R., Kuwahara, M. (eds) *Simulation*

Approaches in Transportation Analysis. Operations Research/Computer Science Interfaces Series, vol 31. Springer, Boston, MA.

[12] Malekzadeh, M., Manolis, D., Papamichail, I., & Papageorgiou, M. (2022, October). Empirical investigation of properties of lane-free automated vehicle traffic. In 2022 IEEE 25th International Conference on Intelligent Transportation Systems (ITSC) (pp. 2393-2400). IEEE.

[13] S. P. Hoogendoorn and P. H. Bovy, "State-of-the-art of vehicular traffic flow modelling", Proceedings of the Institution of Mechanical Engineers, Part I: Journal of Systems and Control Engineering, vol. 215, no. 4, pp. 283–303, 2001.

[14] M. Papageorgiou and A. Kotsialos, "Freeway ramp metering: An overview", in Intelligent Transportation Systems, IEEE, 2000, pp. 228–239.

[15] Messmer, A., & Papageorgiou, M. (1990). METANET: A macroscopic simulation program for motorway networks. *Traffic engineering & control*, 31(9).

[16] Wardrop, J. G., & Whitehead, J. I. (1952). Correspondence. some theoretical aspects of road traffic research. *Proceedings of the institution of civil engineers*, 1(5), 767-768.

[17] May, A. D., & Keller, H. E. (1967). Non-integer car-following models. *Highway Research Record*, 199(1), 19-32.

[18] Papageorgiou, M., Blosseville, J. M., & Hadj-Salem, H. (1989). Macroscopic modelling of traffic flow on the Boulevard Périphérique in Paris. *Transportation Research Part B: Methodological*, 23(1), 29-47

[19] Lighthill Michael James and Whitham Gerald Beresford. 1955 On kinematic waves II. A theory of traffic flow on long crowded roads Proc. R. Soc. Lond. A229317–345

[20]. Daganzo, C. F. (1994). The cell transmission model: A dynamic representation of highway traffic consistent with the hydrodynamic theory. *Transportation research part B: methodological*, 28(4), 269-287.

- [21] Ngoduy D, Maher MJ (2012) Calibration of second order traffic models using continuous cross entropy method. *Transp Res Part C* 24:102–121.
- [22] Spiliopoulou, A., Papamichail, I., Papageorgiou, M., Tyrinopoulos, Y., & Chrysoulakis, J. (2017). Macroscopic traffic flow model calibration using different optimization algorithms. *Operational Research*, 17, 145-164.
- [23] Singer, S., & Nelder, J. (2009). Nelder-mead algorithm. *Scholarpedia*, 4(7), 2928.
- [24] Spiliopoulou, A., Kontorinaki, M., Papageorgiou, M., & Kopelias, P. (2014). Macroscopic traffic flow model validation at congested freeway off-ramp areas. *Transportation Research Part C: Emerging Technologies*, 41, 18-29.
- [25] Troullinos, D., Chalkiadakis, G., Manolis, D., Papamichail, I., & Papageorgiou, M. (2021, September). Lane-free microscopic simulation for connected and automated vehicles. In 2021 IEEE International Intelligent Transportation Systems Conference (ITSC) (pp. 3292-3299). IEEE.
- [26] Troullinos, D., Chalkiadakis, G., Manolis, D., Papamichail, I., & Papageorgiou, M. (2022, September). Extending SUMO for lane-free microscopic simulation of connected and automated vehicles. In SUMO Conference Proceedings (Vol. 3, pp. 95-103).

